Z. Phys. Chem. **222** (2008) 433–469 / **DOI** 10.1524/zpch.2008.222.2–3.433

Computer Simulations of Phase Transitions and Dynamics in Confined Systems

By Heiko Rieger[1,*], Raja Paul[2], Jae-Dong Noh[3], and Grégory Schehr[4]

[1] Universität des Saarlandes, Theoretische Physik, Pf 151150, D-66041 Saarbrücken, Germany
[2] BIOMS/IWR, Universität Heidelberg, Im Neuenheimer Feld, D-69120 Heidelberg, Germany
[3] Department of Physics, The University of Seoul, Seoul 130-743, South Korea
[4] Laboratoire de Physique Theorique d'Orsay, Univ. Paris-Sud 11, 91405 Paris Cedex, France
(Received April 26, 2007; accepted June 25, 2007)

Monte-Carlo Simulations / Non-Equilibrium Dynamics / Nanopores / Orientational Transition / Disordered Systems

Results of theoretical studies of spatially confined systems *via* Monte Carlo simulations are reported. Three experimentally relevant systems are considered: 1) Ad- and desorption phenomena in nanoporous materials like Vycor glass; 2) Dipolar molecules on a graphite surface that undergo an orientational transition; 3) Non-equilibrium dynamics in two-dimensional disordered materials.

1. Introduction

Monte Carlo simulations are an important tool for the theoretical study of phase transitions and dynamics in confined system. The confinement can either be dimensionally, as in the case of surfaces and interfaces, or geometrically by small lateral sizes, as in the case of pores and micro- or nano-crystals. The advantage of computer simulations is that the system size in any spatial direction can easily be varied – a fact that is also systematically used in finite size scaling to study phase transitions of infinite systems.

A number of experimental setups studied in this SFB can be mapped onto statistical physics models that are perfectly suited for a theoretical investigation *via* computer simulations. One is ad- and desorption phenomena in nanoporous materials like Vycor glass, which can be described by grand canonical lattice gas models in special geometries. Another is dipolar molecules on

* Corresponding author. E-mail: h.rieger@mx.uni-saarland.de

a graphite surface that undergo an orientational transition, which we argue to be in the same universality class as the transition(s) occurring in the 6-state clock model on the fully frustrated triangular lattice. For both cases we performed a detailed numerical study, which we report here. In addition we investigated intensively the non-equilibrium dynamics in several two-dimensional disordered materials, which we also review here.

2. Condensation phenomena in nano-pores

Adsorption and desorption isotherms of a gas condensed into nano-pores show hysteresis and have become a very useful tool for the classification of porous materials [1–3]. Due to the effect of surface tension the formation of meniscii inside the pore is delayed on the desorption branch, resulting in a non-vanishing hysteresis area of the sorption isotherms. A theoretical analysis and detailed description of the early research on this phenomenon is described in a review by Everett [4]. Recent investigation from a point of view of the stability of adsorbed multilayers [5] and other [6–8] analytical and numerical approaches together with density functional theory also proposed that the hysteresis phenomenon is an intrinsic property of the phase transition in a single idealized pore and arises from the existence of metastable states. Although real nano-porous materials consist of an interconnected network of simple pores [9, 10], quite recently it has been shown by numerical analysis [11] and experiments [12–14] that hysteresis can occur in isolated pores also. Moreover the shape of the hysteresis loops are influenced by the characteristic features of the pore geometry.

Here we seek insight into the non-equilibrium dynamics in general and the adsorption/desorption hysteresis in particular, within a SINGLE nano-pore – on the basis of a microscopic model. Using extensive Monte Carlo simulations, we characterize the sorption isotherms for different pore geometries and compare our results directly to the experimental observations. Moreover we get insight into the mechanism for the extremely slow dynamics in the confined geometry of a single pore during adsorption and desorption processes as well as during domain growth. We study the phase separation kinetics of a binary liquid in nano-pores at low temperatures. The demixing transition of a binary fluid within a solid gel has been investigated in [15]. Other works [16–18] showed that a binary liquid, unlike Ising-like complete phase separation, does not separate into two phases completely. Instead the adsorbed material forms many small domains far inside the coexistence region.

It has been suggested that this behavior is a consequence of a random pore geometry and can be understood on the basis of the random field Ising model (RFIM) [19–21]. However, Monette *et al.* [22] argued that this picture does not apply to Vycor, with much lower porosity than gels. These are the sys-

tems we are interested in and we focus mainly on isolated (single) pores with a homogeneous wall-particle potential.

A very slow segregation dynamics (as also predicted within the RFIM picture) takes place in single-pores without randomness because the confinement in a small pore slows down domain growth in certain regions of the wetting phase diagram [22] and as a result macroscopic phase separation is not observed on short time scales. Moreover, the late stage domain evolution, obtained from a two point correlation function $C(r, t)$ follows the same Lifshitz–Slyozov [24] growth law of $t^{1/3}$. Unlike earlier works [25] on domain evolution in porous networks, we concentrate on a single pore which is more applicable for systems with low porosity (Si mesopores [14]). Randomness in terms of an irregular pore structure or presence of impurity atoms in the pore wall, which is inherent in real systems, may nevertheless have a substantial effect on the domain growth. An average over many isolated pores corresponding to an assembly of non-interconnected (unlike Vycor) pores, as we consider it in this paper, was experimentally realized [14] by a B-doped Si wafer *via* electrochemical etching.

2.1 Simulation model

A standard model for a binary liquid mixtures is the Ising lattice-gas model with spin occupancy variables $\sigma_i = 0, 1$ governed by the Hamiltonian:

$$\mathcal{H} = -W_{\mathrm{pp}} \sum_{\mathrm{bulk}\langle i,j\rangle} \sigma_i \sigma_j - W_{\mathrm{wp}} \sum_{i \ \mathrm{n.n.\ of\ wall}} \sigma_i \,, \tag{1}$$

where W_{pp} and W_{wp} are the particle–particle and wall–particle couplings, respectively. We denote an occupied site as a particle and an empty site as a vacancy. Experimental observations suggest that in case of a glass (Si) adsorbent, the pore wall has a very strong affinity towards the adsorbed gases, which implies $W_{\mathrm{wp}} > W_{\mathrm{pp}}$. Most of our simulations, unless otherwise specified, are performed at a fixed "wettability" $W_{\mathrm{wp}}/W_{\mathrm{pp}} = 1.5$. A change in this value does not qualitatively affect our results as long as $W_{\mathrm{wp}} > W_{\mathrm{pp}}$. We set $W_{\mathrm{pp}} = 1$ which also defines the units in which energies and temperatures (devided by k_{B}) are measured). The geometry of the simple pore (see Fig. 1a) is chosen to be a rectangle of size $L \times h$ in two dimension and parallelepiped of size $L \times h \times h$ in three dimension with $h \ll L$. The unit in which lengths are measured is one lattice constant. An ink-bottle pore (see Fig. 1b) consists of two simple pores of unequal radii h_1 and h_2. Standard conserved order parameter dynamics (Kawasaki) is employed to study the diffusion and the domain growth kinetics in the nano pores. A spin σ_i at site i chosen randomly and exchanged with one of its nearest neighbor spin σ_j at site j, with Metropolis acceptance probability

$$P(\{\sigma\} \longrightarrow \{\sigma'\}) = \min\left[1, \ \frac{\exp(-\beta\mathcal{H}\{\sigma'\})}{\exp(-\beta\mathcal{H}\{\sigma\})}\right], \tag{2}$$

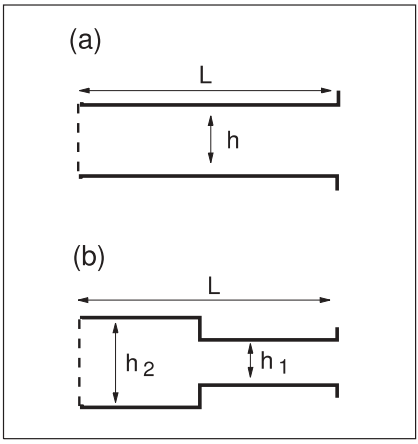

Fig. 1. Schematic representation of (a) simple pore and (b) ink-bottle pore. The dotted line indicates that the pore may be open from both ends.

where σ and σ' represents the old and new spin configuration, respectively. In order to avoid ineffective exchange moves between empty sites we make a list of all occupied sites (particles) and choose up-date sites randomly from this list. 1 MC step contains a number of trial-updates which is equal to the total number of particles actually present in the system and constitutes the unit in which time is measured.

2.2 Hysteresis

To study hysteresis in the adsorption/desorption process within a pore we attach one or two reservoirs depending upon the geometry of the pore. To avoid asymmetric diffusion into the pore, no periodic boundary condition is applied between the reservoirs. The particle density in the reservoirs is kept constant by adding (removing) a particle at a randomly chosen position in the reservoir as soon as a particle diffuses into the pore (reservoir). A snapshot of the hysteresis phenomenon for a simple pore geometry in 2d is shown in Fig. 1. Initially, both the pore and the reservoirs are kept empty. The density of particles in the reservoirs (ρ_{res}) are then slowly increased. Particles are immediately adsorbed and form a single layer along the pore walls. At this stage the density in the pores (ρ_{f}) rises sharply to a non-zero value which corresponds to the first jump of adsorption isotherms (Fig. 2). Then ρ_{f} forms a long plateau until two semicircular (or hemispherical in 3d) meniscii (a meniscus for one-end open pore) are formed somewhere in the middle of the pore at a high reservoir density and move apart from each other to fill the entire pore; a second jump in ρ_{f} is observed. We call this complete pore filling and further increase in ρ_{res} does not change ρ_{f}.

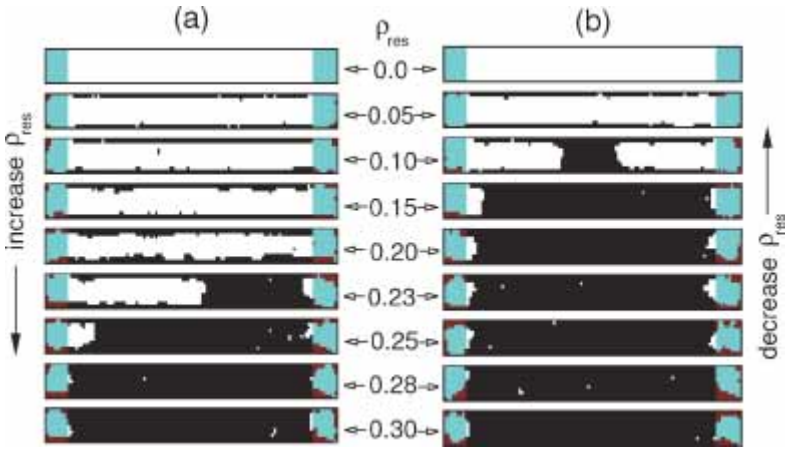

Fig. 2. Snapshots of the hysteresis in a simple nano-pore of size $L = 100$ and $h = 11$ at temperature $T = 0.3$. The shaded regions and the black spots on both sides of the pore are respectively the attached reservoirs and the particles in it. For each value of ρ_{res} the system is equilibrated up to $t = 2^{22}$. Snapshots (a) correspond to the adsorption and (b) correspond to the desorption isotherms.

Next, we slowly decrease the reservoir density and record the corresponding filling fraction ρ_{f} after the system is equilibrated. On desorption, however at a much smaller reservoir density ρ_{res}, we see the semicircular meniscii to form on the open ends of the pore, followed by a sharp fall in the pore density ρ_{f}, as the meniscii approaches towards each other. Finally the desorption curve follow the same path as that of the adsorption. Since the diffusion into the pores is very slow, a long waiting time t_{w} is needed to equilibrate the whole system for each value of ρ_{res}.

Our simulation results are shown in Fig. 2 where the columns (a) and (b) show the hysteresis in 2 and 3 dimensions, respectively. The simulations are performed with systems of length $L = 100$ and 50 at temperatures $T = 0.3$, 0.6 in 2d and 3d, respectively. Reservoir lengths are kept fixed at $L_{\text{r}} = 10$. Ink-bottle pores are equally divided into two parts; one with the narrow tube of diameter h_1 and the other is relatively wider sack with diameter h_2. To make sure that the pore density ρ_{f} does not change any more, each data point of the sorption-isotherms is equilibrated for $t_{\text{w}} = 2^{22}$ time steps. Finally for each hysteresis loop data are averaged over 50 ensembles. It is evident from the sorption branches of Fig. 3 (i)–(iii)a and b, that they are much steeper than in Fig. 3 (i)a and b. This is due the formation of one menuscus on each side of the pore, which accelerates the filling and emptying procedure. Such characteristic feature distinguishes between a one-end open and both-end open pore. Further, an increase in pore diameter requires a higher reservoir density to initiate the formation of meniscii, which effectively delays the onset of adsorption satura-

tion. As a result the the loop area for bigger pore is also increased as shown in Fig. 3 (ii)a and b and (iii)a and b. This features can be used to compare pores of different sizes.

Experimentally [14] one observes a two step decrease of the desorption isotherms for ink-bottle pores. Our data, as shown in Fig. 3 (v)b, for a both-end open pore in 3d of similar geometry, agrees with this experimental observation. The two step decrease of the desorption isotherm arises from the sequential emptying of the different sections (of diameter h_1 and h_2) of the pore. The heights of the two steps suggest that the wider section of the pore emptied earlier than the smaller section. However, the one end open ink bottle geometry Fig. 3 (iv)b does not show this two-step feature, in contrast to the experimental finding [14]. There the two-step feature for ink-bottle pores vanishes only for much smaller temperatures, when the adsorbent is already in the solidphase. Since the temperature is the same in Fig. 3 (iv)b and (v)b a possible reason for the discepancy we find could be that our system sizes and the ratio h_2/h_1 are too small to detect this feature. In 2d ink-bottle pores we do not observe a two step process at all, neither when only one end is open, Fig. 3 (iv)a, nor when both ends are open, Fig. 3 (v)a.

2.3 Evaporation

If a partially or completely filled pore is kept in vacuum, the density inside it decreases with time. This is what we call evaporation and investigate it for different pore geometries. In experiments [14] one measures the vapor pressure change inside a previously equilibrated pore subject to the pressure variation in the reservoir. However, we carry out the simulation in a slightly different way by keeping the initial pore density just above the desorption threshold.

To study the variation in pore density ρ_{f} as a function of time we fill pores completely and allow it to evaporate in an empty reservoir (vacuum). The change in ρ_{f} has been recorded as a function of time t. Decay of the pore density can be very well described by a stretched exponential law,

$$\rho_{\mathrm{f}}(t) \sim \exp\left[-(t/\tau)^{\beta}\right] . \tag{3}$$

The simulations are carried out for pores with both simple and ink-bottle geometry. For the simple pore we study the evaporation at temperature $T = 0.4$, for systems with $L = 128$, 256, 400, 512 and $h = 7$ and finally average over 50 ensembles. The pore density ρ_{f} as a function of time t is plotted in Fig. 4a in a log-linear scale. It is noticed that a pure stretched exponential decay is found only above a certain value of the pore filling fraction as shown by continuous lines. These values of ρ_{f} are nothing but the ratio between the number of surface to bulk molecules and decreases as L becomes larger. The surface molecules are attached rather strongly ($W_{\mathrm{wp}} > W_{\mathrm{pp}}$) to the walls and slow down the evaporation rate for a while but finally drop off suddenly to zero. As the length of the system is increased, the particles deep

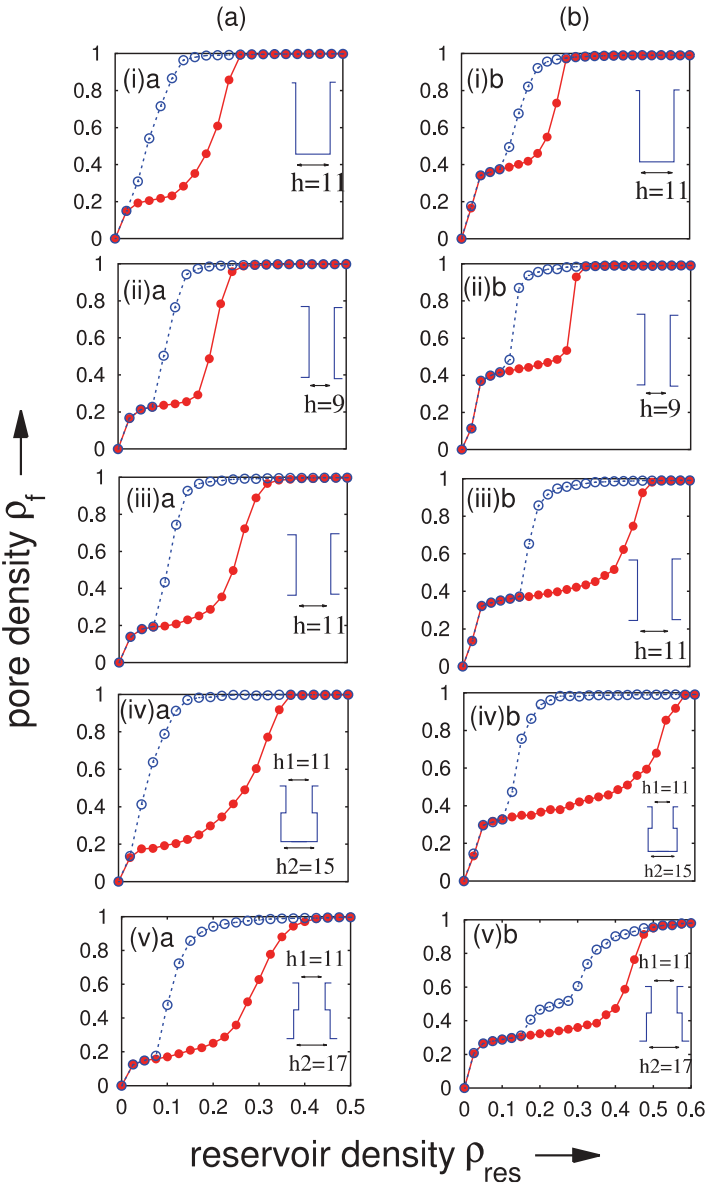

Fig. 3. Adsorption (filled circles) and desorption (empty circles) isotherms for nano pores. (a): Filling fraction ρ_f of the pore as a function of the reservoir density ρ_{res} in 2 dimension. The equilibration time t_w for each data point 2^{22}. (i) has one reservoir of length 10 attached to the open end. II, III and IV have one reservoir attached on each side. (b): Hysteresis isotherms in 3 dimension. Equilibration time $t_w = 2^{22}$, pore length $L = 50$ and reservoir length is 10. For each hysteresis isotherm data are averaged over 50 disorder samples.

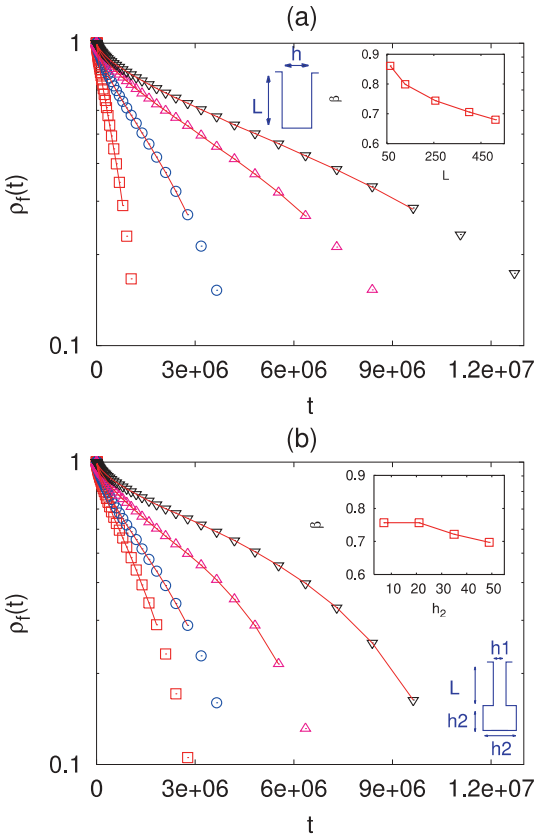

Fig. 4. (a): Evaporation from simple pores of diameter $h = 7$ and different lengths $L =$ 128, 256, 400 and 512 from left to right at temperature $T = 0.4$. Data for the filling fraction $\rho_f(t)$ are shown in a log-linear scale – note that the decay is initially slower than exponential. The full line connects the data points that can very well be fitted to a stretched exponential with the exponent β given in the *inset*. Inset: The decay exponent β as a function of the pore length L. (b): $\rho_f(t)$ for ink-bottle pores of fixed length $L = 200$, tube diameter $h_1 = 7$ at $T = 0.4$ for different sack width $h_2 = 7$, 21, 25, 49 from left to right. The decay law is similar to the simple pores. Inset: β as a function of h_2.

inside the pore requires much more trial attempts to diffuse till the open end which effectively increases the evaporation time for longer pores. This leads to the decay exponent β to decrease with L, as shown in the *inset* of (a).

A similar study in case of ink-bottle pores was carried out with systems of fixed $L = 200$ and $h_1 = 7$ for different values of $h_2 = 7$, 21, 35, 49 as shown in Fig. 4b. The temperature is kept fixed at $T = 0.4$ and data are averaged over 50 ensembles. Like the previous case, here also, ρ_f shows a pure stretched

exponential decay above a certain value, which becomes smaller as h_2 is increased. Moreover the effective length $(L + h_2)$ of the pore increase with h_2 results in the decay exponent β (*inset* of (b)) to drop off similarly to the simple pore. A further analysis (not shown) on both simple and ink-bottle pore shows that β is independent of the temperature.

2.4 Domain evolution and random walks

In this section we study the temporal evolution of domain structures inside pores starting with a random (high temperature) initial configuration of given density. Now we use periodic boundary conditions between the two ends of the pore and the total number of particle is conserved. Figure 5a, shows the domain structure-profile at different time steps when the system is quenched to $T = 0.3$ from $T = \infty$. Fig. 5b is the snap-shot of a cut along the pore axis. The black regions correspond to the occupied sites and are called "particle-domains", whereas empty white regions are termed "blobs".

In the initial stage, the growth is dominated by nucleation and spinodal decomposition. As soon as the domain- or the blob-size becomes comparable to the diameter of the pore, the above two mechanisms do not work any more. Transverse directional growth is completely stopped because of the pore wall and the horizontal movement of the blobs is slowed down by the presence of the particle-domains.

The snapshots in Fig. 5 confirm that the random motion of the blobs plays an important role in the late stage of growth. A closer look to Fig. 5b, which is horizontally the occupancy along the pore-axis and vertically time in log scale, shows in the late stage, the blobs move to and fro along the axis of the pore and penetrate through the particle-domains to coalesce with the neighbors. During this process it also transfers a holes (vacancies, white regions) from its surface to the neighboring blobs.

To elucidate the random motion, we study the time evolution of a single blob as shown in Fig. 5c. Initially it is a perfect rectangle of linear size (l_b) comparable to the pore diameter (h) and placed in the center of the pore. The temperature is kept fixed at $T = 0.3$. The system is allowed to evolve and the mean square deviation $\langle x^2(t)\rangle$ of the center of mass (COM) of the blob along the axis of the pore is measured at each time step. Since the boundary of the blob perpendicular to the wall, fluctuates very rapidly, the true COM may not lie on the geometrical axis of the pore. In this case we trace the actual COM and project it on to the axis. The size of the blob has to be chosen large enough to avoid disintegration of the main blob.

Since we start with an exactly rectangular blob, a true random-walk motion is not immediately observed. In the early stages, the blob walls, perpendicular to the pore axis roughens, leading to $\langle x^2(t)\rangle \sim t^{2/3}$ as in surface roughening described by the KPZ-equation [26]. At late stages ($t > 10^4$), the blob performs

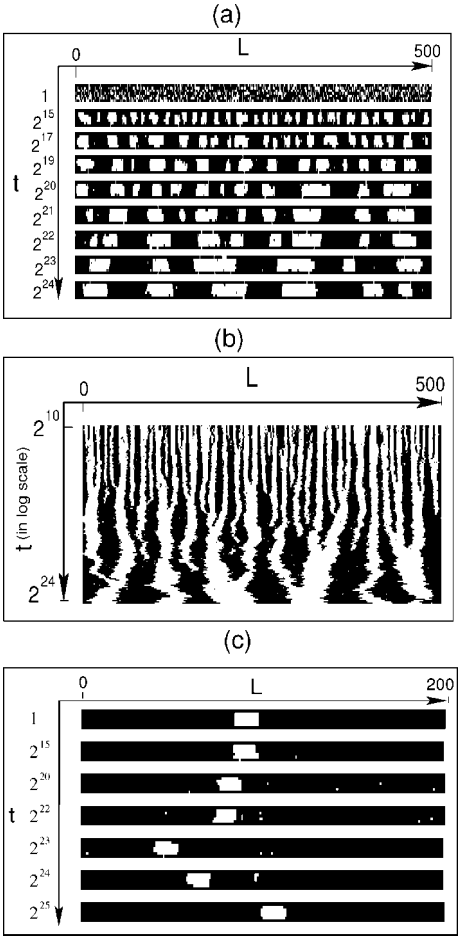

Fig. 5. (a): Domain evolution in nano-pores. The figures are produced by taking snap-shot for a system of length $L = 300$ and height $h = 7$ at temperature $T = 0.3$. (b): Axial snap-shot of the domains for the same system in Fig. a. A horizontal cut through the figure at any instant t will give the location and size of domains/blobs along the axis of the pore. The time is plotted in logarithmic scale. (c): Time evolution of a single rectangular blob of linear size $l_b = 13$ in a pore of dimension 200×7 at $T = 0.3$.

a random walk with a blob-size dependent diffusion constant $\mathcal{D}(l_b)$,

$$\langle x^2(t)\rangle = \mathcal{D}(l_b)\, t\,. \tag{4}$$

Fig. 6a, shows the mean square displacement $\langle x^2(t)\rangle$ of the COM of blobs with $l_b = 11, 15, 19, 23, 27, 31, 35, 39$ as a function of time t. For each values of l_b the simulation is carried out in a system with fixed $L = 200$, $h = 7$ at

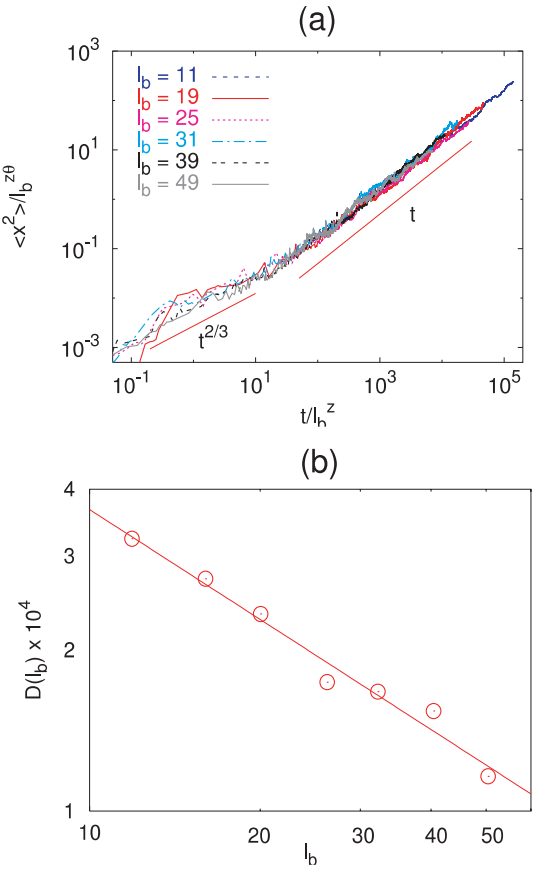

Fig. 6. (a): Mean-square deviation of blobs of size $l_b = 11, 15, 19, 23, 27, 31, 35, 39$ for a system size $L = 200$, $h = 7$ and the temperature $T = 0.3$. **(b)**: Shows the power low decay of the diffusion constant $\mathcal{D}(l_b)$ for different blob sizes. The exponent is found to be $\gamma = 0.68$.

temperature $T = 0.3$ and finally averaged over 1000 ensembles. It is evident from the figure that the onset of a true random-walk is delayed for bigger blobs. A scaling form for both small and large time scale regime is,

$$\langle x^2(l_b, t)\rangle \propto \tau^{\theta}(l_b)\ f(t/\tau(l_b))\,, \tag{5}$$

with

$$f(x) \sim \begin{cases} x^{\theta} & \text{for } x \ll 1 \\ x & \text{for } x \gg 1. \end{cases} \tag{6}$$

Assuming, $\tau(l_b) \sim {l_b}^z$, from Eq. (5), one can write for large time $t \gg \tau$,

$$\langle x^2(l_b, t)\rangle \propto {l_b}^{z(\theta-1)}\, t\,, \tag{7}$$

which readily gives,

$$\mathcal{D}(l_b) \sim l_b^{-z(1-\theta)} = {l_b}^{-\gamma}\,. \tag{8}$$

The scaling form in Eq. (5) gives quite reasonable data collapse for $\theta = 2/3$ and $z = 2$, as shown in Fig. 5a. Substituting these value in Eq. (8) we obtain the value of $\gamma = 2/3$. Diffusion constant $\mathcal{D}$ evaluated from the asymptotic behavior [*cf.* Fig. 5a] is plotted in Fig. 5b. From the slope of $\mathcal{D}$ *vs.* l_b curve in log–log scale we estimate the $\gamma = 0.68$ which agrees quite well with the previous value $2/3$, obtained from the scaling. Note that the relation $\mathcal{D} \propto 1/l_b^{2/3}$ deviates from the naive expectation $\mathcal{D} \propto k_B T\eta/l_b$ [22, 23], where k_B, T, η are the Boltzmann's constant, temperature and viscosity coefficient of the medium, respectively.

2.5 Discussion

Using extensive Monte Carlo simulations we have shown how hysteresis arises in nano-pores for different pore structures. The characteristics of the sorption branches are influenced by the shape and size of the pore geometry. Since the hysteresis in nano-pores occur due to diffusion, the temperature has to be chosen very carefully to avoid a slow diffusion rate at low temperatures or a vanishing hysteresis-loop at high temperatures. The absence of a two-step desorption branch in 2d ink-bottle pores may be due to the effect of a small temperature as found in the experiment [14]. The choice of the pore diameters for one-end open ink-bottle geometry is also an important factor. Because of surface tension effect, a large curvature ratio $\frac{1}{h_1}\Big/\frac{1}{h_2}$, can cause a huge pressure difference between the narrow and wide parts of the pore. Increase in curvature corresponds to a decrease in vapor pressure; described by the Kelvin equation. As an effect if the narrow part of the pore is filled early, can block the particle to diffuse into the wider part, unless a very high density is reached in the reservoir.

The stretched exponential decay of the pore density $\rho_f(t)$ also agrees qualitatively with the experiments [14]. One simple reason of such a behavior of $\rho_f(t)$ could be due to the formation of meniscus at the open end of the pore which eventually restricts the rate of evaporation depending upon the radius of its curvature.

For the phase separation of binary liquids in the pore environment, model B [29] corresponding to dynamics with conserved order parameter, is not well suited, as it does not account for the transport of the order parameter by hydrodynamic flow. Modifications to model B by adding an "advection" term describes the system quite well [30].

The late stage coarsening in the pore system that we studied is effectively driven by two mechanisms: (1) Transfer of holes from the surface of one blob to a neighboring blob and (2) the transfer of particles from one side of the blob to the other along the pore wall. Owing to the first mechanism a blob shrinks and the neighboring blobs grow, whereas due to the second one a blob moves to and fro as a whole and coalesce with another. Our numerical study for a single blob accounts for the contribution arises from (2) only and gives rise to the diffusion constant $\mathcal{D} \sim l_{\mathrm{b}}^{-2/3}$ of a blob of size l_{b}. The first mechanism modifies the single-blob diffusion constant in a non-trivial way, which is difficult to estimate. Finally, the superposition of random motion of blobs due to mechanism (2) and the hole transfer mechanism in (1) leads to a late-stage growth law $R(t) \sim t^{1/3}$, independent of their individual contributions.

The domain growth exponent $1/\psi$, systematically investigated in [28], is significantly decreased in presence of random wall-particle potential W_{wp} which in practice is due to the effect of impurity atoms at the pore walls. The temperature dependence of the exponent may come from a logarithmic scaling [27] of barrier energy of the domains. On the other hand geometrical defects appear to slow down the growth process only in the early time regime. But in the late stage, as the blob size becomes larger than the wave length of the geometrical disorder, which in this case is the periodicity of the wall-defect, the domain growth displays the same behavior as in the case of smooth walls.

3. Frustrated antiferromagnetic six-state clock model on the triangular lattice

Two-dimensional systems cannot show long-range order by breaking a continuous symmetry at any finite temperature T. Nevertheless Kosterlitz and Thouless (KT) demonstrated that the two-dimensional (2d) *XY*-ferromagnet with nearest neighbor interaction and, equivalently, the planar rotator exhibit a phase transition from an ordered phase with an algebraic decay of the spin correlations to a disordered phase *via* the unbinding of vortex–antivortex pairs [31].

The KT-concept has been applied successfully to the onset of superfluidity [32, 33] and of superconductivity [34] in thin films and two-dimensional melting [35]. An application to layered magnetic systems with large ratios of the intra- and the inter-layer exchange appears to be more direct, but here the KT transition is masked by the transition to 3D behavior [36]. In Ref. [64] X-ray diffraction data on CF_3Br monolayers physisorbed on graphite where presented together with evidence that the orientational *pseudospin* ordering is of the KT-type.

Physisorbed monolayers are indeed good approximations to 2d systems, as evidenced by the fact that phase transitions occurring in such layers can be often described by the versions of elementary models of statistical mechanics such as the Ising or the 3-state Potts model [37–39].

The halomethane CF_3Br is a prolate C_{3v} molecule with a fixed dipole moment of about 0.5 D pointing along the threefold axis parallel to the C–Br bond. Clearly the pseudospin correlations are bound to a plane, thus the system is 2d with respect to the relevant degrees of freedom at the phase transition. The pseudospin is presumably not a strictly isotropic planar rotator but experiences a crystal field which breaks the continuous azimuthal symmetry. It has been shown however that – at least for the planar *XY* ferromagnet – the KT-behavior is stable with respect to small crystal fields of 6-fold symmetry [40]. The site symmetry of the monolayers is indeed 6-fold, but the ordered structure approached is not ferro- but antiferroelectric. Antiferro-type ordering on a triangular lattice is affected by frustration with the consequence that the helicity, a discrete 2-fold symmetry, enters into the problem. The order-disorder transition is then described by a confluence of the Ising and KT universality classes [41, 42] with an Ising type anomaly of the specific heat, but the spin correlations of the disordered phase still follow the KT-form of $\xi(T)$ as we will demonstrate now.

From the above considerations follows that the pseudo-spins formed by the CF_3Br dipoles are arranged on a triangular lattice, interact antiferromagnetically with nearest neighbors[1] and have 6 preferred orientations described by an azimuthal angle θ[2]. Hence the model that captures the *universal* features of the orientational ordering transition (*i.e.*, those that are independent of the microscopic details of the interactions between the molecules) should be the anti-ferromagnetic six-state clock model on a 2d $N = L_x \times L_y$ triangular lattice (see Fig. 7). The six-state clock spin is a planar spin pointing toward discrete six directions; $\mathbf{S} = (\cos\theta, \sin\theta)$ with $\theta = \frac{2\pi n}{6}$ $(n = 0, 1, \ldots, 5)$. The Hamiltonian of this model reads

$$\mathcal{H} = 2J \sum_{\langle i,j \rangle} \cos(\theta_i - \theta_j)\,, \tag{9}$$

where the sum is over nearest neighbor site pairs $\langle i, j \rangle$ and $J > 0$ is the antiferromagnetic coupling strength in which here all energies and temperatures (divided by k_B) are measured). The overall factor 2 is introduced for a computational convenience. It is a limiting case of an antiferromagnetic *XY* model with infinite anisotropy field $\cos p\theta$ $(p = 6)$.

The antiferromagnetic coupling on a triangular lattice induces a frustration. As a result the system has 12-fold degenerate ground states with three-sublattice structure. Global spin rotations by multiples of $2\pi/6$ and also Ising

[1] The character of the relevant orientation dependent interactions of CF_3Br is not known, but a comparison of monolayers of several polar methane derivatives [69] suggests that for CF_3Br the short range anisotropic part of the intermolecular van der Waals force and hard core repulsion are more important than the medium range dipole–dipole interaction.

[2] The polar orientation of the normal component of the dipole moments is not resolved by the X-ray diffraction data.

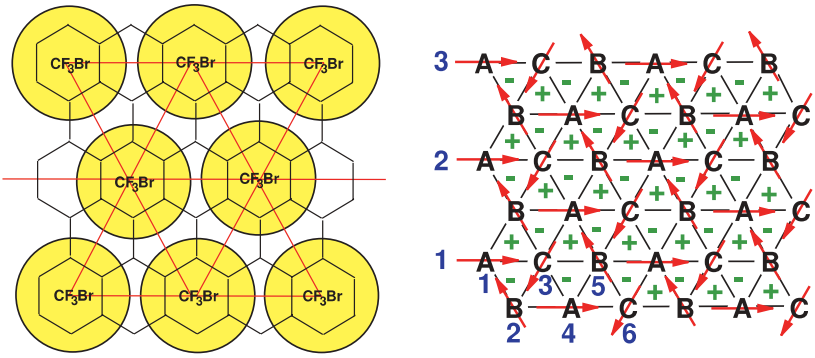

Fig. 7. *Left*: The spatial arrangement of the CF_3Br molecules on the underlying hexagonal graphite surface in the 2×2 structure that is present below 105 K. The resulting trigonal lattice is also shown. *Right*: A triangular lattice of size 12×3 with the 6-state clock spins indicated as arrows representing the 6 preferred directions of the CF_3B dipolar moments. The arrow configuration shown is one of the 12 ground states by which the lattice sites are separated into three *A*, *B*, and *C* sub-lattices. The helicity for each elementary triangle corresponding to this ground state is also indicated by $+$ and $-$.

like transformation that inverts all helicities formed by the spins on elementary triangles (see Fig. 7) transforms one ground state into another. Therefore the model possesses a C_6 (6-fold clock) $\times$ Z_2 (Ising) symmetry and we expect that there are two phase transitions associated with the spontaneous breaking of the C_6 and Z_2 symmetry. Despite a lot of efforts, there is no consensus on the nature of the phase transitions and it is not clear whether the two transitions happen at two different temperatures or at a single one. For instance, the fully frustrated *XY* (FFXY) model, describing an array of Josephson junctions under an external magnetic field [41, 43], has a continuous $U(1)$ symmetry *and* a discrete Ising or Z_2 symmetry that can be broken at low temperatures through a Kosterlitz–Thouless (KT) type transition and an Ising-like transition, respectively.

Renormalization group (RG) studies on the FFXY model drew the conclusion that the transitions occur at the same temperature [44]. Monte Carlo simulation studies on generalized FFXY models supported the single transition picture for the FFXY model [45]. Interestingly, it has been reported that the Z_2 symmetry breaking transition may not belong to the Ising universality class. Monte Carlo studies of the FFXY models on a triangular and a square lattice yielded the correlation length exponent $\nu = 0.83(4)$ (triangular lattice) and $\nu = 0.85(3)$ (square lattice), which is inconsistent with the Ising value $\nu = 1$ [46]. The specific heat appeared to follow a power-law scaling rather than the logarithmic scaling as one would expect for the Ising universality class. A non-Ising scaling behavior is also observed in the studies of the FFXY model *via* a Monte Carlo simulation [47] and Monte Carlo transfer matrix cal-

culations [48, 49]. The same non-Ising critical behavior is also observed in the coupled XY-Ising model [46, 50, 51].

On the other hand, numerical evidence also in favor of two transitions at two different temperatures has been collected. Monte Carlo simulation studies of the frustrated Coulomb gas system, which is supposed to be in the same universality class as the FFXY model, showed that the KT type transition temperature T_{KT} and the Ising-like transition temperature T_{I} are different with $T_{\mathrm{KT}} < T_{\mathrm{I}}$ [52, 53]. Two transitions were also found in the FFXY model on a square lattice [54] and on a triangular lattice [55–57] using Monte Carlo simulations. A careful analysis of the RG flow of the FFXY model also led to a conclusion of the double transition scenario [58]. It is the general belief that the transitions at T_{KT} and at T_{I} belong to the KT universality class [59] and to the Ising universality class, respectively, if the transitions occur at different temperatures. However, the critical exponents associated with the Z_2 symmetry breaking, which are found by Monte Carlo simulations, turn out to be different from those of the Ising universality [53, 54, 57]. They are rather close to those obtained in the XY-Ising model [46]. Although there is an argument that the observed non-Ising exponents are due to a screening effect hindering the asymptotic scaling behavior [60], the controversy on the nature of the phase transition remains unsettled [61–63].

Here we present a thorough numerical study of a related model, the fully frustrated anti-ferromagnetic six-state clock model on a triangular lattice. We also report on an orientational ordering transition in a two-dimensional experimental system [64] that, as we argue, is in the same universality class as the model we study numerically. The experimental system actually motivates (besides numerical simplicity) our restriction to the six states of the spins rather than the continuum XY spins (and thus to a six-fold clock (C_6) symmetry rather than the $U(1)$ symmetry). In the unfrustrated (ferromagnetic) case it has been shown, however, that the KT-behavior is stable with respect to a crystal field of six-fold symmetry [40, 65, 66]. Hence we expect that our model displays the same critical behavior as the FFXY model.

3.1 Symmetries and order parameter

We investigate the phase transitions of the anti-ferromagnetic six-state clock model, defined by Eq. (9), on a two-dimensional $N = L_x \times L_y$ triangular lattice (see Fig. 7). The antiferromagnetic interaction on a triangular lattice induces a frustration. As a result the spins on each triangles should make an angle of $\pm 120^\circ$ with one another in the ground state. There are 12-fold degenerate ground states with three-sublattice structure. According to their chirality, we can categorize the ground states into $\mathcal{C}_n$ and $\mathcal{A}_n$ ($n = 0, 1, \ldots, 5$). The spin configurations in each ground state are given by

$$\theta_{i\in A} = \frac{2\pi n}{6}\,, \quad \theta_{i\in B} = \frac{2\pi(n\pm 2)}{6}\,, \quad \theta_{i\in C} = \frac{2\pi(n\pm 4)}{6}\,, \tag{10}$$

for $\mathcal{C}_n$ (upper sign) and $\mathcal{A}_n$ (lower sign). In other words, in the $\mathcal{C}(\mathcal{A})$ type ground state, the spin angles increase by $\frac{2\pi}{3}$ along the up-triangles in the (anti-) clockwise direction, and *vice versa* for down-triangles.

There are two different symmetries between them; those in the same class of $\mathcal{C}$ or $\mathcal{A}$ are related by the rotation $\theta_i \to \theta_i + \frac{2\pi m}{6}$ ($m = 0, \ldots, 5$) and those in the others by the reflection $\theta_i \to -\theta_i$. Therefore the model possesses the C_6 (six-fold clock) symmetry and the Z_2 (Ising) symmetry. Note that the FFXY model on a triangular lattice has a $U(1)$ and a Z_2 symmetry [41]. Since the clock spin can have only six states, while the XY spin is a continuous one, the continuous $U(1)$ symmetry of the FFXY model is reduced to the discrete C_6 symmetry. The nature of the Z_2 symmetry in each model is identical.

From the symmetry consideration, we expect that there are two types of phase transitions associated with the spontaneous breaking of the C_6 symmetry and the Z_2 symmetry. The chirality at each elementary triangle is defined as

$$h_{\triangle_i,\triangledown_i} = \frac{2}{3\sqrt{3}}\left[\sin(\theta_j-\theta_i)+\sin(\theta_k-\theta_j)+\sin(\theta_i-\theta_k)\right] ,$$

where $\triangle_i$ and $\triangledown_i$ are up- and down-triangles as depicted in Fig. 7. Then the ground state $\mathcal{C}_n$ ($\mathcal{A}_n$) has a checker-board pattern of the chirality with $h_{\triangle} = +1$ (-1) and $h_{\triangledown} = -1$ $(+1)$. The staggered chirality

$$h = \frac{1}{2N}\sum_i \left(h_{\triangle_i} - h_{\triangledown_i}\right) , \tag{11}$$

plays a role of the order parameter for the Z_2 symmetry breaking transition. The order parameter for the C_6 symmetry breaking transition is the sublattice magnetization

$$m_A = \frac{1}{N}\sum_{i\in A} \exp(i\theta_i) , \tag{12}$$

where the sum runs only over the sites in the A sublattice. m_B and m_C are defined analogously.

3.2 Transition temperatures

We performed Monte Carlo (MC) simulations on finite $N = L \times (L/2)$ lattices with a sublattice updating scheme; one of the three sublattices is selected randomly and then all spins in the chosen sublattice are flipped according to the Metropolis rule. One Monte Carlo step corresponds to three sublattice updates. Various observables are measured during the MC runs, such as the energy, the chirality, and the sublattice magnetization, from which we can measure the averaged quantities and their fluctuations. In some cases, histograms are

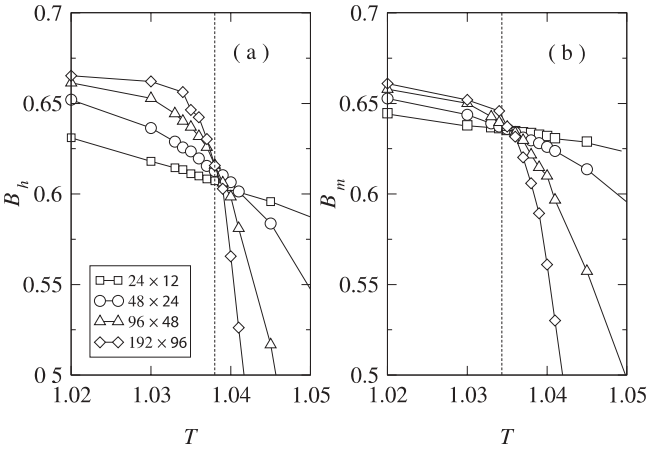

Fig. 8. Binder parameters for the staggered chirality in (a) and the magnetization in (b). The estimated transition temperatures are marked by broken lines.

constructed from particularly long MC runs to obtain the observables as continuous functions of the temperature.

The transition temperature is determined from the Binder parameter

$$B_h = 1 - \frac{\langle h^4 \rangle}{3\langle h^2 \rangle^2} \qquad \text{and} \qquad B_m = 1 - \frac{\langle m_A^4 \rangle}{3\langle m_A^2 \rangle^2} \tag{13}$$

for the chirality and the magnetization, respectively. Here the angle bracket denotes a thermal average, which can be done by a time average over the MC runs. The Binder parameter is scale-independent at the critical points and approaches $\frac{2}{3}$ (0) in the ordered (disordered) phase as L becomes larger. Hence the order–disorder transition temperature $T_{\rm I}$ related to the Z_2 symmetry breaking is obtained from the crossing point in the plot of B_h *versus* T at different system sizes. From Fig. 8a we estimate that

$$T_{\rm I} = 1.038 \pm 0.0005\,. \tag{14}$$

B_m also displays the crossing behavior (Fig. 8b), from which we estimate that

$$T_{\rm KT} = 1.035 \pm 0.0005\,, \tag{15}$$

for the C_6 symmetry breaking transition.

The Binder parameters show different size dependence at low temperatures. For the staggered chirality B_h converges to $2/3$ rapidly as L increases. However, B_m appears to converge to values less than $2/3$ at $T < T_{\rm KT}$. It indicates that there is a quasi-long-range order in spins at $T < T_{\rm KT}$. We confirm it from

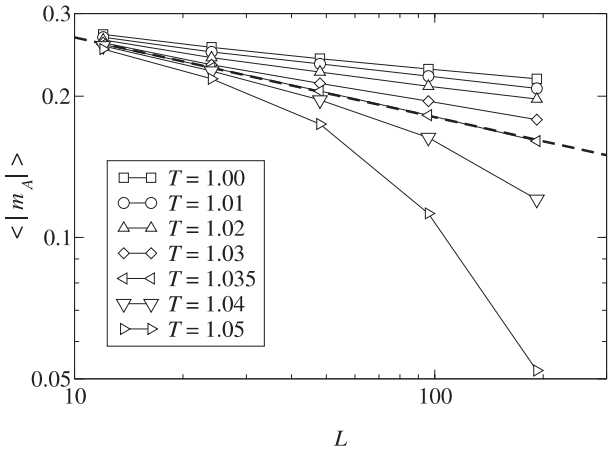

Fig. 9. Sublattice magnetization $\langle |m_A| \rangle$ near the critical temperature T_{KT}. At temperatures $T \leq T_{\mathrm{KT}}$ it shows a power law behavior. The broken line has a slope -0.17.

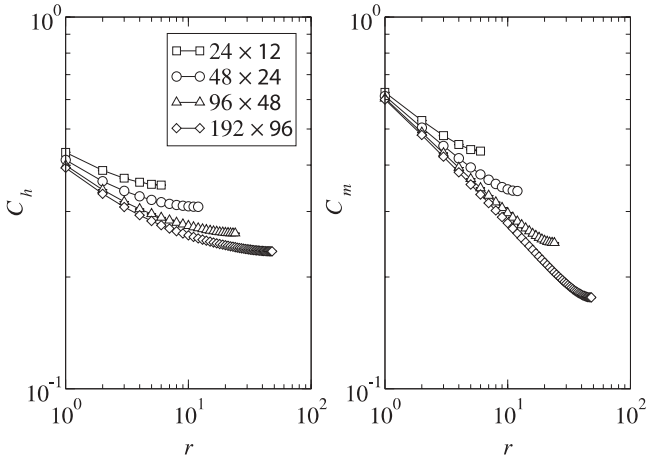

Fig. 10. Correlation functions of the staggered chirality, C_h, and the magnetization, C_m, at temperature $T = 1.037$.

finite-size-scaling (FSS) behaviors of the magnetization. The sublattice magnetization shows the power law scaling behavior, $\langle |m_A| \rangle \sim L^{-x}$, at $T \leq T_{\mathrm{KT}}$ with temperature dependent exponent x (see Fig. 9).

The two transition temperatures lie very close to each other. Nevertheless the accuracy of the data is sufficiently high that we can exclude the possibility that $T_{\mathrm{I}} = T_{\mathrm{KT}}$. Figure 10 demonstrates this *via* the correlation functions. We measure the correlations between the chirality of up-triangles and the magne-

tization of spins in the A sublattice displaced by a distance r in the vertical direction:

$$C_h(r) = \left\langle \frac{3}{N} \sum_{i \in A} h_{\triangle_i} h_{\triangle_{i+r}} \right\rangle , \tag{16}$$

$$C_m(r) = \left\langle \frac{3}{N} \sum_{i \in A} \cos(\theta_i - \theta_{i+r}) \right\rangle . \tag{17}$$

Here, $i+r$ denotes a site displaced vertically by a distance r from i, and $\triangle_i$ denotes an up-triangle whose left corner is i (see Fig. 7). In Fig. 10, we plot both correlation functions in the log–log scale at an intermediate temperature $T = 1.037$. Clearly one can see an upward curvature in the plot of $C_h(r)$, which implies that the chirality order has already set in. On the other hand, there is a downward curvature in the plot of $C_m(r)$ indicating that the magnetic order has not set in yet. Therefore we conclude that $T_{\mathrm{KT}} < T_{\mathrm{I}}$.

3.3 Universality class

With $T_{\mathrm{KT}} \neq T_{\mathrm{I}}$, one expects that both symmetry breakings take place independently. Then, the Z_2 symmetry breaking transition should be in the Ising universality class. The C_6 symmetry is equivalent to that of the XY model perturbed by the $(p = 6)$-fold anisotropy field. The unperturbed XY model displays a KT transition which separates a disordered high-temperature phase and a quasi-long-range ordered low-temperature phase. A renormalization group (RG) study shows that an anisotropy field with $p > 4$ does not change the KT nature of the transition [40]. The same is true for the extreme case of the ferromagnetic six-state clock model [66]. So the C_6 symmetry breaking phase transition at $T = T_{\mathrm{KT}}$ is expected to belong to the KT universality class.

The interplay of the Ising type and the KT type ordering has long been studied in the context of the fully frustrated XY models on a square or a triangular lattice. Frequently, it has been claimed [44–49] that the Ising-like transition and the KT-type transition occur at the same temperature. On the other hand, more recent studies have reported the transitions to occur at two different temperatures [52–58, 60, 61, 63]. Surprisingly, some of recent high-precision Monte Carlo simulation studies suggested that the Z_2 symmetry breaking transition does not belong to the Ising universality class in spite of the double transition [54, 57, 63]. They estimated that $\nu \simeq 0.8$ for the correlation length exponent and $\alpha/\nu \simeq 0.46$ with the specific exponent α, which are incompatible with the Ising values of $\nu = 1$ and $\alpha = 0$. The critical exponents are consistent with the values observed along the single transition line of the coupled XY-Ising model [46, 50, 51]. Olsson [60] argued that the measured non-Ising critical exponents are artifacts of unusual finite size effects originated from

non-critical spin-wave fluctuations. However, apparently there is no general agreement yet on this subject [61].

In our model, we observe the phase transitions occurring at two *different* temperatures. However, the controversy existing in the FFXY model tells us that it does not guarantee necessarily that each transition will belong to the KT universality class and the Ising universality class, respectively. Therefore we perform a thorough finite-size-scaling (FSS) analysis to understand the nature of the phase transition. We believe that the antiferromagnetic six-state clock model can be used to resolve the existing controversy for the FFXY model. It has the proper symmetry properties as discussed previously. And, from a practical point of view, larger system sizes are available since it is a discrete model, with which one can reduce the finite size effects.

3.4 Z_2 symmetry breaking

We investigate the nature of the Z_2 symmetry breaking transition by exploring the FSS property of the specific heat, defined by

$$c = N\left[\langle e^2\rangle - \langle e\rangle^2\right], \tag{18}$$

with e the energy per site. For a finite system ($N = L \times L/2$) the specific heat has a peak $c_* \sim L^{\alpha/\nu}$ near the critical temperature, diverging with system size $L \to \infty$. Since the specific heat does not diverge at a KT type transition, the divergence is due to the Z_2 symmetry breaking phase transition. The Ising universality class has $\alpha = 0$, and the specific heat shows a logarithmic divergence, $c_* \sim \ln L$.

From a detailed analysis [67] of the specific heat and the chirality correlation length $\xi_h = \sqrt{\sum_r r^2 C_h(r)/\sum_r C_h(r)}$, with $C_h(r)$ defined in Eq. (16), we conclude that the Z_2 symmetry breaking transition belongs to the Ising universality class. Our results for the *effective* specific heat exponent $\alpha/\nu \simeq 0.5$ and the correlation length exponent $\nu \simeq 0.8$ appearing at small length scale are comparable with the results of previous MC works claiming the non-Ising nature in the frustrated XY models [46, 47, 50, 51, 54, 57, 62, 63]. Our results are fully consistent with Olsson's argument claiming that the non-Ising exponents reported by others are explained by a failure of finite-size-scaling at small length scale due to the screening length associated with the nearby KT transition [60]. The strong finite size effect is overcome in this work since we could study large systems. We expect that one could observe the same crossover to the asymptotic Ising type scaling behavior in larger scale simulations in the frustrated XY systems.

3.5 C_6 symmetry breaking

The KT transition is characterized by the essential singularity of the correlation length and the susceptibility approaching the critical temperature. We measure

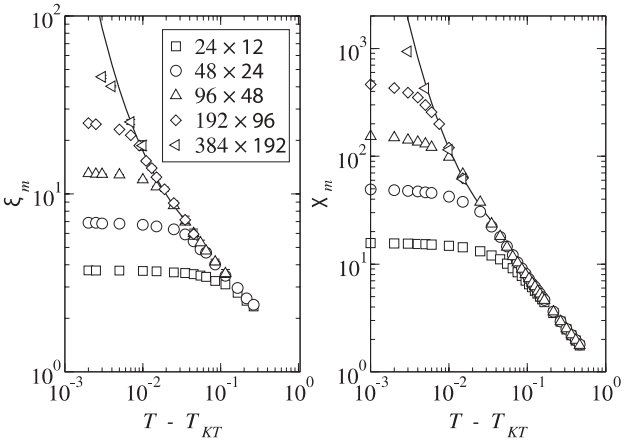

Fig. 11. Correlation length and the susceptibility of the magnetization. The solid lines are the fits to the KT form of $\xi_m = 2.54\mathrm{e}^{0.193(T-T_{\mathrm{KT}})^{-1/2}}$ and $\chi_m = 4.20\mathrm{e}^{0.333(T-T_{\mathrm{KT}})^{-1/2}}$.

the correlation length ξ_m as

$$\xi_m = \sqrt{\frac{\sum_{\mathrm{r}} r^2 C_m(r)}{\sum_{\mathrm{r}} C_m(r)}}\,, \tag{19}$$

from the magnetic correlation function C_m in Eq. (17). One can also estimate the correlation length by fitting $C_m(r)$ to a form with e^{-r/ξ_m}. We tried with various function forms but found that Eq. (19) yields the most stable estimate against statistical errors. The magnetic susceptibility is measured from the fluctuation of the magnetization, $\chi_m = N\langle m_A^2\rangle$. Figure 11 shows the plot of ξ_m and χ_m *versus* $T - T_{\mathrm{KT}}$ in log–log scale. Upward curvature in both plots indicates the stronger divergence than the algebraic divergence. We fit those quantities with the KT scaling form, $\xi_m = a\ \mathrm{e}^{b(T-T_{\mathrm{KT}})^{-y}}$ and $\chi_m = a'\mathrm{e}^{b'(T-T_{\mathrm{KT}})^{-y}}$ with $y = \frac{1}{2}$ fixed, whose results are drawn with solid lines in Fig. 11. It shows that the KT scaling behaviors are emerging only after $L \geq 96$. If y is also taken as a fitting parameter, one obtains $y < 0.5$ whose value depends on the fitting range; it increases as approaching the critical temperature.

In the XY phase ($T < T_{\mathrm{KT}}$) the spins have the quasi-long range order; the magnetization scales algebraically as $\langle |m_A| \rangle \sim L^{-x}$ with temperature dependent exponent x (see Fig. 9). The RG theory predicts that $x = 1/8$ at the KT transition point [40]. Our numerical data show that $x \simeq 0.17$ at $T = T_{\mathrm{KT}}$. We think that the discrepancy originates from a sensitive dependence of x on T. In summary, in spite of a quantitative disagreement, the C_6 symmetry breaking phase transition is in qualitative agreement with the KT universality class; we observe the essential singularity in the correlation length and the susceptibility and quasi-long range order in the low temperature phase.

3.6 Experimental realization: CF_3Br on graphite

In this section we describe a possible experimental realization of the theoretical model we investigated above. In a recent work we reported results on X-ray powder diffraction study on a monolayer of halomethane CF_3Br adsorbed on exfoliated graphite [64]. CF_3Br is a prolate molecule and has a dipole moment of about 0.5 D. The coverage ρ, temperature T phase diagram is rather complex [68, 69]. In [64] we concentrated on a coverage which is representative of the extended monolayer regime in which the monolayer lattice is commensurate with the graphite lattice. This yields a 2×2 triangular lattice arrangement of the CF_3Br molecules below a temperature of 105 K [70], which is the melting temperature of the commensurate layer. The inter-molecular distance is $a = 4.92$ Å. Note that the lateral size of the graphite crystallites is only around 180 Å, which confines any spatial correlation length to this value.

An isolated CF_3Br would prefer to lie flat on the substrate, but the 2×2 mesh is too tight to accommodate the molecules in this orientation. Therefore the individual CF_3Br molecules stand on the substrate, presumably with the F_3 tripod down, with a maximum tilt angles of the molecular axis up to 30° with respect to the substrate normal due to steric repulsion. A tilt leads to a non-zero in-plane component of the dipole moment. We regard this component as planar pseudospin $\mathbf{S}_i = (\cos\theta_i, \sin\theta_i)$ with the azimuthal angle θ_i of the molecule. In this sense the 2×2 state is disordered with a zero time average of every $\mathbf{S}_i$, and is stabilized at higher temperatures by a libration and/or a precession of the molecular axis about the substrate normal.

As the temperature is decreased additional features develop in the diffraction pattern which finally, below 40 K, can be identified [64] as Bragg peaks (with a finite width of around $(180\,\text{Å})^{-1}$ due to the lateral size of the crystallites) indicating an orientational order in the dipole moments identical to the one depicted in Fig. 7. The temperature dependence of the correlation length ξ, determined from the intrinsic width of this peak, can be fitted with the KT-expression

$$\xi = A \exp(B(T/T_{\text{KT}} - 1)^{-1/2}) \tag{20}$$

to the data for $T > 40$ K (see Fig. 3 of Ref. [64]). The fit parameters are $A = 9 \pm 2$ Å, $B = 1.5 \pm 0.4$, $T_{\text{KT}} = 30 \pm 3$ K. Note that the value of A is reasonably close to the lattice parameter of the 2d mesh. Thus ξ is expected to diverge at a KT-critical temperature T_{KT} of about 30 K, but the growth of the correlated regions is interrupted when ξ reaches the size of the graphite crystallites. This happens at about 40 K.

We think that the model of Eq. (9) is a good description of the orientational ordering process described in this physical system: Clearly the pseudospin correlations are bound to a plane, thus the system is 2d with respect to the relevant degrees of freedom at the phase transition. Moreover, as mentioned before, below 105 K the CF_3Br molecules are arranged in a triangular lat-

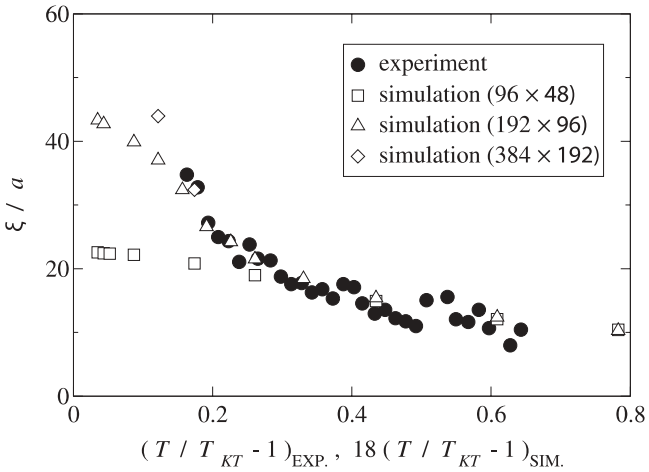

Fig. 12. Comparison of the magnetic correlation length (scaled by the lattice constant) from the experimental data (from Fig. 3 of Ref. [64]) and the Monte Carlo simulations (from Fig. 11). The reduced temperature $(T/T_{\mathrm{KT}} - 1)$ for the simulation data are rescaled by a factor of 18 in order to achieve an acceptable data collapse for linear lattice sizes L between 96 and 192.

tice. The pseudospin representing the CF_3Br dipole moment is presumably not a strictly isotropic planar rotator but experiences a crystal field from the graphite substrate which breaks the continuous azimuthal symmetry into the six fold symmetry of the monolayer. This is reflected by the six-state clock variables of model (9). The ordered structure of the CF_3Br dipoles is antiferroelectric, which is taken into account by the antiferromagnetic couplings between the pseudospins in Eq. (9). Finally, the character of the relevant orientation dependent interactions of CF_3Br is not known, but a comparison of monolayers of several polar methane derivatives [69] shows that fully halogenated molecules including CF_3Br with small dipole moments around 0.5 D have structures different from partially halogenated molecules such as CH_3Cl with strong dipole moments around 1.7 D. This suggests that for CF_3Br the short range anisotropic part of the intermolecular van der Waals force and hard-core repulsion are more important than the medium range dipole–dipole interaction. Thus the interactions can be assumed to be short ranged. Thus one expects that model (9) and the physical system discussed here are in the same universality class.

In Fig. 12 a comparison of the magnetic correlation length from the experiment [64] and the simulation (from Fig. 11) is shown. Since the factor B in the KT-form (20) of the correlation length is a non-universal number the reduced temperature $(T/T_{\mathrm{KT}} - 1)$ has to be rescaled by an appropriate factor in order to achieve an acceptable data collapse. The rescaling factor turns out to be quite large, namely 18, which is not unusual for microscopically different systems in

the KT universality class (see *e.g.*, [71]). Note that the finite linear size of the crystallites plays a similar role as the finite lattice sizes in the simulations and sets the saturation value for the correlation length (divided by the lattice constant for the triangular lattice of the CF_3Br molecules, which is $a = 4.92$ Å). The nice collapse of the experiment and simulation data supports our claim that the two physical systems are in the same universality class and that the orientational ordering of CF_3Br molecules on graphite is in the KT universality class.

3.7 Summary

To summarize we have studied the phase transitions in the anti-ferromagnetic six-state clock model on a triangular lattice, which is fully frustrated. As a result the ground states have a C_6 (six-state clock) symmetry and a Z_2 (Ising) symmetry. Through extensive Monte Carlo simulations we found that the model undergoes a Kosterlitz–Thouless transition at T_{KT} and an Ising transition at T_{I}. The two transitions correspond to the C_6 and the Z_2 symmetry breaking transition, respectively. High-precision Monte Carlo data indicate that the two transitions take place at different temperatures, $T_{\mathrm{KT}} < T_{\mathrm{I}}$ (Eqs. (14) and (15)). This has been checked explicitly by analyzing the behavior of the spin and the chirality correlation function at temperatures between T_{KT} and T_{I} (Fig. 10). Furthermore, we have shown that the Z_2 symmetry breaking transition belongs to the Ising universality class. For small system sizes, the scaling property of the specific heat and the correlation length deviates apparently from the Ising universality class. However, simulation results for larger system sizes indicate that the model belongs asymptotically to the Ising universality class. As for the transition at T_{KT}, we have found that the magnetization correlation length and the susceptibility diverges at $T = T_{\mathrm{KT}}$ according to the KT scaling form (Fig. 11). We have also found that the spins have a quasi long range order below T_{KT} (Fig. 9). Combining these, we conclude that the transition at T_{KT} belongs to the KT universality class.

Our model is a variant of the fully frustrated XY models where the KT type ordering and the Ising type ordering interplay interestingly. Our numerical results support a scenario that there are two separate phase transitions with $T_{\mathrm{KT}} \neq T_{\mathrm{I}}$; one at T_{KT} in the KT universality class and the other at T_{I} in the Ising universality class. Our results are consistent with those in Ref. [60] very well.

We have proposed that our theoretical model describes the orientational ordering transition of CF_3Br molecules on graphite since the model has the same symmetry as the experimental system. We argue that the orientational ordering transition belongs to the KT universality class [64] by comparing the magnetic correlation length obtained from the experiment [64] with the correlation length obtained numerically in the six-state clock model. With a suitable rescaling of parameters, we have shown that the correlation lengths in both sys-

tems have the same scaling behavior (Fig. 12). It gives more evidence that the orientational ordering transition is indeed the KT transition.

4. Growing length scales during aging in 2d disordered systems

The non-equilibrium dynamics of disordered, in particular of glassy systems has become a very rich field in recent years and despite many efforts the understanding of non-equilibrium dynamics of disordered and glassy systems in finite dimensions remains a challenging problem. In particular in glasses and spin glasses the aging process displays a very rich phenomenology demanding new theoretical concepts [72]. But already less complex – and apparently less glassy – systems, like disordered but non-frustrated systems [73] or even pure systems [74] reveal interesting and unexpected aging phenomena. One of the most intriguing questions in this context is whether the out-of-equilibrium dynamics is essentially fully determined by a coarsening process (a question that even arises in the more complex spin glass situation [75]), describable by a growing length scale that characterizes essentially all out-of-equilibrium processes. In this paper we will consider three paradigmatic models for two-dimensional systems with quenched disorder with a focus on existence and analysis of a growing length scale during aging at low temperatures: the random bond Ising ferromagnet, the Edwards Anderson model for a spin glass, and the solid-on-solid model on a disordered substrate which is equivalent to the sine-Gordon model with random phase shifts.

4.1 The random bond Ising ferromagnet

As the first example for two-dimensional disordered system we consider the random bond Ising ferromagnet. It is defined by the Hamiltonian

$$H = -\sum_{(ij)} J_{ij} S_i S_j, \quad S_i = \pm 1\,, \tag{21}$$

where the couplings J_{ij} are non-negative quenched random variables of variance ε and the sum is over all nearest neighbor pairs (ij) on a square lattice of size $L \times L$ with periodic boundary conditions. This paradigmatic model for a disordered magnetic system (with bond- or temperature randomness) with an Ising symmetry has a second order phase transition from a paramagnetic to a ferromagnetic phase at a critical temperature $T_c(\epsilon)$ that decreases with increasing disorder strength ϵ. For temperatures T below T_c the magnetization $\overline{\langle m_i \rangle_T}$, where $\langle \cdots \rangle_T$ means the thermal average and $\overline{\cdots}$ the average over the disorder, takes on a non-vanishing value. Temperature is measured in the same unit as energy (divided by k_B).

Non-equilibrium dynamics at temperatures below T_c arises for instance *via* an instantaneous quench of the systems from the paramagnetic phase to

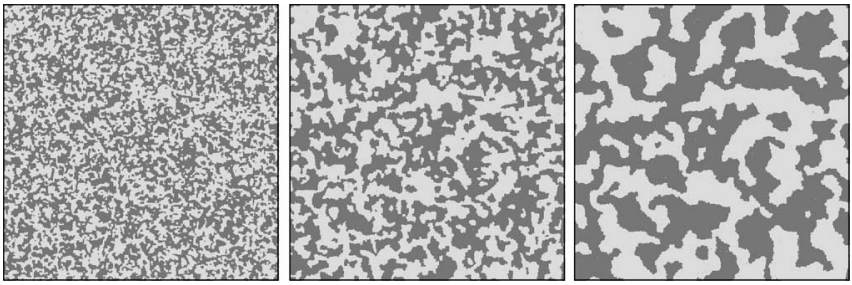

Fig. 13. Domain growth in the RBIM with Glauber kinetics. We show evolution pictures at $t = 10^2$, 10^4 and 10^6 MCS for a 512×512 lattice, after a quench from $T = \infty$ to $T = 0.5$ and J_{ij} uniformly distributed between 0 and 2 ($J_{ij} \in [0, 2]$). The up spins are marked in black, and the down spins are marked in grey.

a temperature below T_c. A stochastic process defined by single spin–flip transition rates defined for instance by the Metropolis rules $w(S_i \to -S_i) = 1/(1 + \exp(-\beta(H(S_i) - H(-S_i))))$ models a non-conserved order parameter dynamics and can be studied by computer simulations. For a quench below T_c the dynamics is a coarsening process during which ferromagnetic domains of a typical lateral extension $R(t)$ form, where t is the time elapsed after the quench (see Fig. 13). A standard way to extract this time dependent length scale is *via* the spatial two-point correlation function $C(r, t) = \overline{\langle m_i(t) m_{i+r}(t) \rangle_T}$, which is expected to scale like $C(r, t) = \tilde{c}(r/R(t))$.

An important study of the non-conserved RBIM is due to Huse and Henley (HH) [76]. HH argued that coarsening domains are trapped by energy barriers $E_B(R) \simeq E_0 R^{\psi}$, with exponent $\psi = \chi/(2 - \zeta)$, where χ and ζ are the pinning and roughening exponents. For $d = 2$, these exponents are known to be $\chi = 1/3$ and $\zeta = 2/3$ [77], yielding $\psi = 1/4$. As a consequence of the HH scenario one expects the following scaling scenario for the length scale $R(t)$:

$$R(t)/R_0 = h(t/t_0)\,, \quad \text{with} \quad h(x) \sim \begin{cases} x^{1/2} & \text{for } x \ll 1 \\ (\ln x)^4 & \text{for } x \gg 1 \end{cases}\,, \tag{22}$$

where $R_0 \sim T^4$ and $t_0 \sim T^8$. Instead we find (*via* an extensive Monte Carlo study, see [78]) that $R(t)$ grows algebraically with a temperature and disorder strength dependent exponent $1/z(T, \epsilon)$:

$$R(t) \sim t^{1/z(T,\epsilon)} \quad \text{for} \quad t \gg t_0 \quad \text{with} \quad z(T, \epsilon) = 2 + \epsilon/T\,, \tag{23}$$

where the time t_0 does not depend on T and ϵ (see Fig. 14). This algebraic growth law with a temperature and disorder strength dependent growth exponent θ indicates a logarithmic barrier scaling form $E_B(R) \sim \epsilon \ln(1 + R)$ in contrast to the algebraic form $E_B \propto R^{\psi}$ assumed in the HH picture.

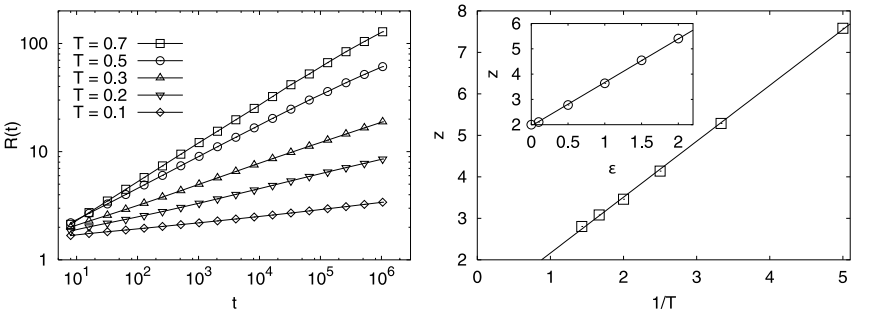

Fig. 14. *Left:* Log–log plot of the correlation length R *vs.* time t in the 2d random bond Ising model for different temperatures and $J_{ij} \in [0, 2]$. *Right*: Estimates of the exponent z *vs.* $1/T$ for the data shown left (note that for $T > 1 \approx T_c$, *i.e.* for $1/T < 1$ the system is in the paramagnetic phase). Inset shows z *vs.* the disorder strength ϵ for fixed temperature $T = 0.5$ (the distribution $P(J)$ is chosen to be uniform over $[1 - \epsilon/2, 1 + \epsilon/2]$. The straight lines (in the main figure and in the inset) represent the analytical prediction $z = 2 + \epsilon/T$.

4.2 2d EA spin glass

Here we consider the two-dimensional Ising spin glass with nearest-neighbor interactions distributed according to a Gaussian with zero mean and variance one

$$H = -\sum_{\langle ij \rangle} J_{ij} S_i S_j \,, \quad \text{with} \quad P(J_{ij}) = \frac{1}{\sqrt{2\pi}} \exp\left(-\frac{J_{ij}^2}{2}\right) . \tag{24}$$

This model is in a paramagnetic state for all temperature $T > 0$ but displays a very slow dynamics at low temperatures which can be observed for instance in the non-equilibrium dynamics occurring after a quenched from high temperatures. It turns out [79] that this aging process can be characterized by a coarsening process up to a maximum domain size given by the equilibrium correlation length $\xi_{\rm eq}$.

It is possible to calculate exactly the ground state (GS) of this system using for instance a minimal weight perfect matching algorithm [80]. Denoting the GS for a particular disorder realization with $\{S_i^0\}$ we define the local overlap with it as $q_i^{\rm gs}(t) = S_i(t) S_i^0$. For a ferromagnetic system (*i.e.* $J_{ij} = J > 0$) the GS obviously $S_i^0 = 1$ and therefore q_i corresponds to the (time dependent) local magnetization. In Fig. 15 snapshots of the time evolution of the local GS overlap are depicted, showing an increasing average domain size. In contrast to the time evolution of a random bond ferromagnet shown in Fig. 13 even for very large waiting times very small domains exist. These are either very stable clusters because strong bonds have to be broken to flip the spins or new domains within the bigger ones appear since less strongly bound spins initialize the formation of a new domain.

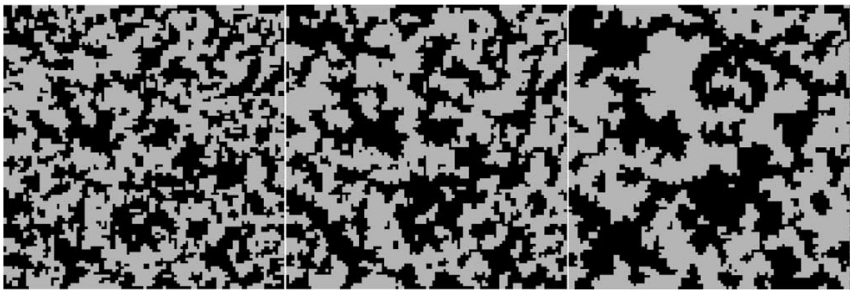

Fig. 15. Domain growth in the 2d EA-model with Gaussian couplings for $T = 0.3$. The system size is $L = 100$, *i.e.* much smaller than in Fig. 13. The snapshots show the domains relative to the ground state after $t = 10^2$, 10^4 and 10^6 Monte Carlo sweeps.

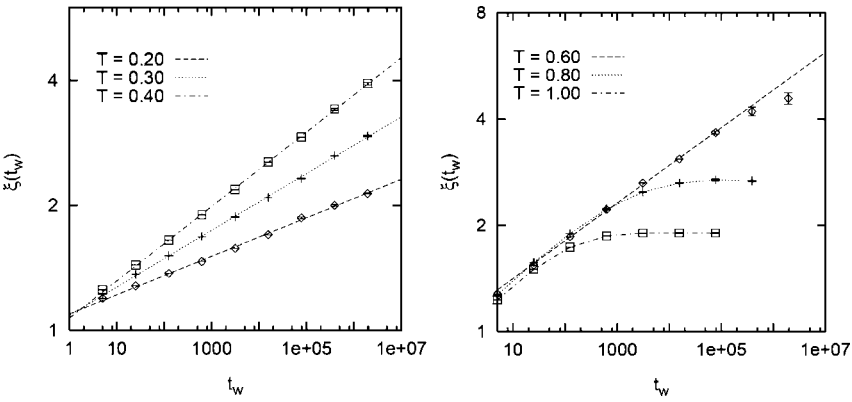

Fig. 16. Correlation length in the 2d EA SG model as a function of time t_w for different temperatures. *Left*: Fits to an algebraic growth law $\xi(t_w) \sim t^{1/z(T)}$ with $1/z(T = 0.2) = 0.046$, $1/z(T = 0.3) = 0.068$ and $1/z(T = 0.4) = 0.090$. *Right*: For sufficiently large temperatures the time dependent correlation length $\xi(t)$ saturates at the equilibrium correlation length $\xi_{\rm eq}(T)$ within the accessible time window.

The spatial correlation function

$$G(r, t) = \overline{\langle q_i^{\rm gs}(t) q_{i+r}^{\rm gs}(t) \rangle} \tag{25}$$

allows for a quantitative analysis of the domain size evolution. It turns out that it scales like $G(r, t) = g(r/\xi(t))$ and we can obtain an estimate for the correlation length (or typical domain size) *via* an integral of $G(r, t)$ over r. The result is shown in Fig. 16. Note that for increasing temperatures a) the domain growth speeds up, b) the equilibrium correlation length gets smaller. As a consequence of both tendencies one can observe the saturation of the time dependent corre-

lation length at the finite equilibrium correlation length for higher temperatures on the right panel.

We observe that the data for $\xi(t)$ (in the non-equilibrium regime $\xi(t) \ll \xi_{\rm eq}(T)$) can very well be fitted by an algebraic growth law with a temperature dependent exponent $z(T)$:

$$\xi(t) \propto t^{1/z(T)} \quad \text{with} \quad z(T) \approx (0.23T)^{-1}\,, \tag{26}$$

which displays again the $1/T$ behavior that we have encountered already in the last section for the random bond ferromagnet, indicating also here the presence of logarithmic barriers.

4.3 2d SOS model on a disordered substrate

Here, we investigate the non equilibrium relaxational dynamics of a solid-on-solid (SOS) model on a disordered substrate, defined on a two dimensional square lattice and described by the following elastic Hamiltonian in terms of height variables h_i

$$H_{\rm SOS} = \sum_{\langle ij \rangle} (h_i - h_j)^2\,, \quad h_i \equiv n_i + d_i\,, \tag{27}$$

where n_i are unbounded discrete variables, *i.e.* $n_i \in \{0, \pm 1, \pm 2, \dots\}$ and $d_i \in [0, 1[$ are uniformly distributed quenched random offsets, uncorrelated from site to site. In the absence of disorder, *i.e.* $d_i = 0$, the model exhibits a roughening transition in the same universality class as the Kosterlitz–Thouless transition [81], at a temperature $T_{\rm r}$ separating a flat phase at low T from a logarithmically (thermally) rough one above $T_{\rm r}$. The presence of disorder is known to modify significantly the nature of the transition [82]. The so-called *super-roughening* transition occurs at a temperature $T_{\rm g} = T_{\rm r}/2 = 2/\pi$. Above $T_{\rm g}$, where the disorder is irrelevant on large length scales, the surface is logarithmically rough again, although below $T_{\rm g}$ the system exhibits a glassy phase where the pinning disorder induces a stronger roughness of the interface.

The spatial (2-point) connected correlation function is defined as

$$C(r, t) = \frac{1}{L^2} \sum_i \overline{\langle h_i(t) h_{i+r}(t) \rangle - \langle h_i(t) \rangle \langle h_{i+r}(t) \rangle}\,, \tag{28}$$

which scales as

$$C(r, t) = \mathcal{F}\,(r/\mathcal{L}(t)) \quad \text{with} \quad \mathcal{L}(t) \sim t^{1/z}\,. \tag{29}$$

Therefore one can estimate $\mathcal{L}(t)$ by integrating $C(r, t)$ over r. In Fig. 17 we show the value of $\mathcal{L}(t)$ computed in this way for different temperatures. One obtains a rather good fit by a power law $\mathcal{L}(t) \sim t^{1/z(T)}$, thus obtaining a value

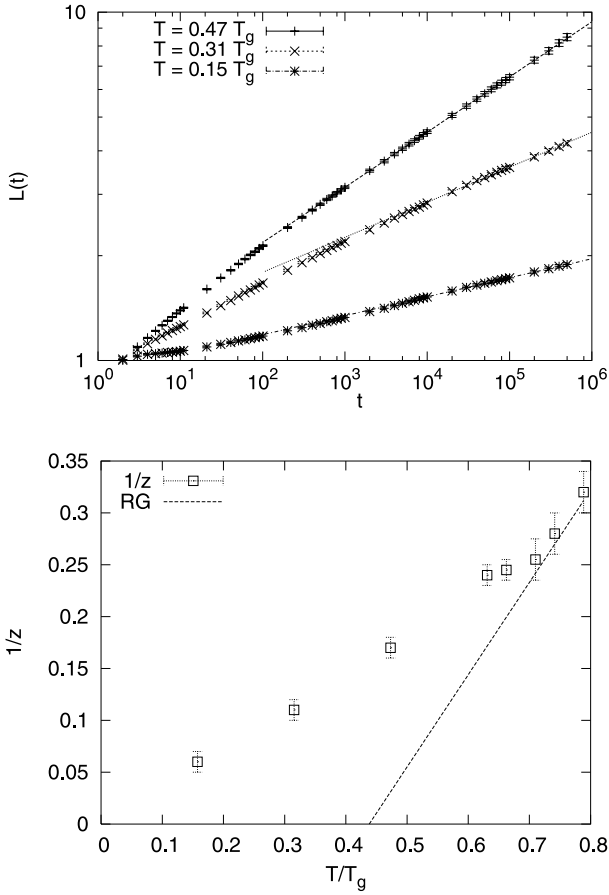

Fig. 17. *Left*: Growing length scale $\mathcal{L}(t)$ for different temperatures. The solid lines are guides to the eyes. *Right*: $1/z(T)$ as a function of T/T_{g}. The dashed line which shows the result of the one loop RG is drawn without any fitting parameter.

of the T dependent dynamical exponent. One notices also that $\mathcal{L}(t)$ approaches an algebraic growth after a pre-asymptotic regime which increases with decreasing temperature. Figure 17 shows our estimate for $1/z(T)$ as a function of T (for details see [84]. As expected, the dynamical exponent is a decreasing function of the temperature. One expects that $z = 2$ for $T > T_{\mathrm{g}}$ and that it becomes T-dependent below T_{g} with $z = 2 + 2\mathrm{e}^{\gamma_E}\tau + \mathcal{O}(\tau^2)$ as predicted by a one loop RG calculation [83]. At high temperature $T > T_{\mathrm{g}}$ and in the vicinity of T_{g}^-, it is numerically rather difficult to extract a reliable estimate for the dynamical exponent due to finite size effects. Therefore we restrict ourselves here to lower temperatures $T < 0.8\,T_{\mathrm{g}}$. For temperature $T \gtrsim 0.7\,T_{\mathrm{g}}$, the value of z is still in reasonable agreement with the RG prediction. Around the value

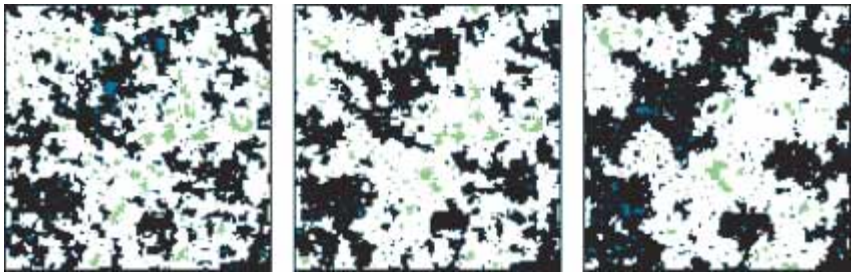

Fig. 18. Snapshot of the height field of the random SOS model relative to the ground state $m_i(t) = n_i(t) - n_i^0$ for $T = 0.47\,T_g$. The system site is $L = 128$. Different colors correspond to different values of $m_i(t)$: $m_i(t) = -2$ in green, $m_i(t) = -1$ in white, $m_i(t) = 0$ in black and $m_i(t) = +1$ in blue. Note that large domains in white and black persist and change only slowly in time.

$T^* \simeq 0.63\,T_g$, where $z \simeq 4$, the curve $1/z(T)$ shows an inflection point, below which $1/z$ decreases linearly with T. In this regime, $z(T)$ is well fitted by

$$z(T) \approx 4T^*/T \quad \text{for} \quad T \leq T^* \approx 0.63 T_g\,. \tag{30}$$

The behavior $z \propto 1/T$ is compatible with an activated dynamics over logarithmic barriers, *i.e.* an Arrhenius type behavior $t_{typ} \sim e^{B_{L\,typ}/T}$ with $B_{L_{typ}} \sim \log L_{typ}$.

One may try to relate the length scale $\mathcal{L}(t)$ to the size of spatially correlated structures like domains or droplets. We first explored the idea that at low temperature, the nonequilibrium dynamics could be understood as a coarsening process reflected in a spatially growing correlation with the ground state (GS). Interestingly, computing the GS of the SOS model on a disordered substrate Eq. (27) is a minimum cost flow problem for which a polynomial algorithm exists and can therefore be computed exactly [85]. After determining one GS n_i^0 (note that the GS, which is computed with free boundary conditions, is infinitely degenerate since a global shift of all heights by an arbitrary integer is again a GS), we define for each time t the height difference $m_i(t) = n_i(t) - n_i(0)$ and identify the connected clusters (domains) of sites with identical $m_i(t)$ using a depth-first search algorithm. Notice that for the comparison with the ground state, the Monte Carlo simulations are performed here using free boundary conditions.

In Fig. 18 we show snapshots of these domains for $T < T_g$. Starting from a random initial configuration one can for $T < T_g$ very quickly ($t \lesssim 100$) identify large domains that evolve only very slowly at later times. On the other hand for $T > T_g$ the configurations decorrelated very quickly in time. To make this analysis more quantitative, we determined the cluster size distribution $P_{th}(S, t)$ for one realization of the disorder (and for different realizations of the thermal noise).

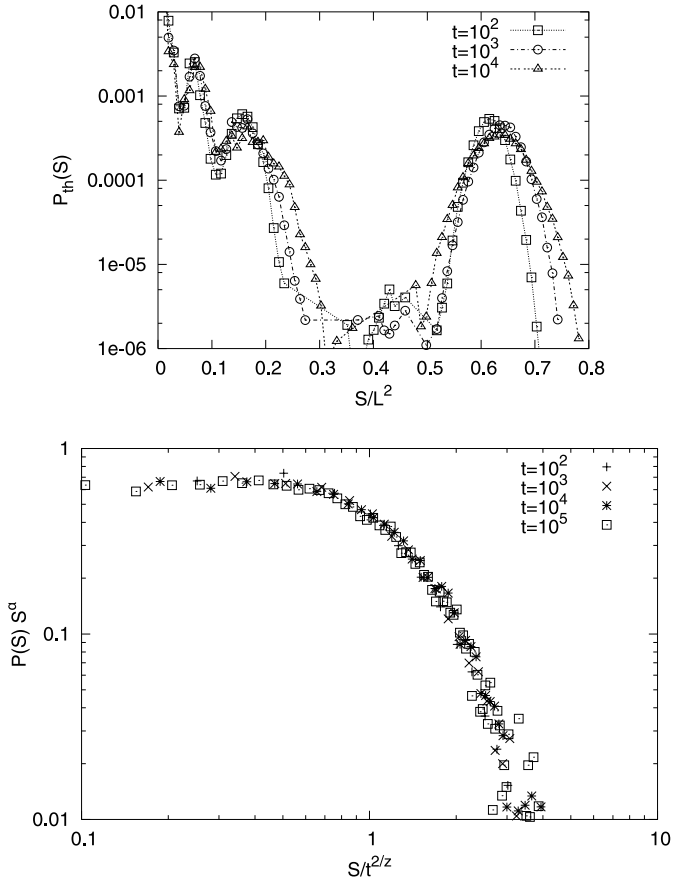

Fig. 19. *Left*: Size distribution $P_{\rm th}(S,t)$ (see definition in the text) for different times t. Here $T = 0.47 T_{\rm g}$. *Right*: $S^{\alpha} P^{\rm GS}_{\rm droplet}(S,t)$ with $\alpha = 1.9 \pm 0.1$ as a function of $S/t^{2/z}$ with $2/z = 0.26 \pm 0.03$. Here the initial condition is the ground state and $T = 0.3\, T_{\rm g}$.

As shown on Fig. 19, $P_{\rm th}(S,t)$ starts to develop a peak at a rather large value $S^*(t)$ on the earlier stage of the dynamics (this peaks also develops if we start with a random initial configuration). It turns out that $S^*(t)$ is the size of the largest connected flat cluster of the ground state configuration $n_i^0 = C^{\rm st}$. On the time scales presented here, as time t is growing, this peak remains stable $S^*(t) \simeq C^{\rm st}$, implying that the system is *not* coarsening. At later times, as suggested by simulations on smaller systems, this peak progressively disappears and the distribution becomes very flat. We also checked that the mean size of these connected clusters is not directly related to $\mathcal{L}(t)$. One has however to keep in mind that we are computing the *connected* correlation functions, *i.e.* we measure the thermal fluctuations of the height profile around its mean

(typical) value $\langle h_i(t)\rangle$. Therefore, we believe that these connected correlations are instead related to the broadening of this "stable" peak (Fig. 19), *i.e.* the fluctuations around this typical state at time t.

To characterize more precisely the fluctuations around this cluster, we identify "droplets" by initializing the system in the ground state itself $n_i(t=0) = n_i^0$. At low temperature, and on the time scales explored here, one expects that the ground state represents a good approximation of a typical configuration, *i.e.* $\langle n_i(t)\rangle \simeq n_i^0$. We compute the distribution $P^{\rm GS}_{\rm droplet}(S,t)$ of the sizes of the connected clusters with a common value of $m_i(t) \neq 0$. It turns out, as shown in Fig. 19, that $P^{\rm GS}_{\rm droplet}(S,t)$ obeys the scaling form

$$P^{\rm GS}_{\rm droplet}(S,t) = \frac{1}{S^\alpha}\mathcal{F}^{\rm GS}_{\rm droplet}\left(\frac{S}{\mathcal{L}^2(t)}\right), \quad \alpha = 1.9 \pm 0.1\,, \tag{31}$$

where α is independent of T within the accuracy of our data and $\mathcal{L}(t) \sim t^{1/z}$. The value of z in (31) is in good agreement with the one extracted from the 2-point correlation function $C(r,t) = F(r/\mathcal{L}(t))$ Eq. (29).

4.4 Conclusion

We studied the time dependent correlation length $R(t)$ in three models of disordered systems in two dimensions that are characterized by distinct features: 1) The random bond Ising ferromagnet as an example for a random system that has long range order at low temperatures and is expected to perform a simple (but slow) coarsening process after a temperature quench into the ordered phase. 2) The Edwards–Anderson spin glass model as an example for a frustrated system without a finite temperature critical point and an ordered phase but with an extremely slow dynamics and a large correlation length at very low temperatures. 3) The disordered SOS model as a model with a critical point and a low temperature phase without long range order but infinite correlation length. Surprisingly, in spite of the pronounced differences between these systems we find that all three show an algebraic dependence of the correlation length on the age t of the system $R(t) \sim t^{1/z(T)}$ and that the exponent z (which would be identical to the dynamical exponent if the system is critical) depends linearly on the inverse temperature:

$$z(T) \propto 1/T\,. \tag{32}$$

IF the dynamics at low temperatures in all 3 systems is thermally activated this behavior hints at a logarithmic scaling behavior of the energy barriers as a function of their size. In the disordered SOS model one would actually expect such a scaling [84]. For the EA spin glass (in 2d) the situation is complicated by the fact that the ground state is not expected to be stable with respect to thermal fluctuations, *i.e.* in principle excitations of increasing size would cost less and

less energy – therefore a logarithmic barrier scaling comes a bit as a surprise. Finally for the random bond Ising model a simple scaling picture [76] based on the scaling behavior of the domain walls in this model would predict an algebraic energy scaling – resulting in a formally infinite value for z, which is not confirmed by our results [78]. Hence we have to conclude with the observation that the common behavior Eq. (32) of the growth exponent z in 2d disordered models indicates a more complicated and yet hidden mechanism that is active in the non-equilibrium dynamics of these systems at low temperatures at least during the first 10 decades of the aging process.

We also would like to emphasize the fact that the physical interpretation of the growing length scale in the three systems under consideration in this paper is quite different: In the random bond ferromagnet it is simply the typical transverse domain size, where domains are easily identified as connected clusters of common magnetization sign. In the EA spin glass model the length scale is also determined by a domain size – where domains where defined as connected clusters of spins with common orientation with respect to one of the two ground states. These domains grow steadily up to a maximum size set by the equilibrium correlation length. In the disordered SOS model, however, the growing length scale is *not* connected to growing domains – actually the system settles quite fast after the temperature quench into a configuration that has a pretty large overlap with one of the ground states. Instead of growing further these initially very large domains thermal fluctuations of increasing size destroy these domains – and it is the spatial extent of these fluctuations that is characterized by the growing length scale studied here.

References

1. F. Rouqerol, J. Rouqerol, and K. Sing, *Adsorption by Powders and Porous Solids*. Academic Press, New York (1999) Chapt. 7.
2. K. S. W. Sing, D. H. Everett, R. A. W. Haul, L. Moscou, R. A. Pierotti, J. Rouqerol, and T. Siemieniewska, Pure Appl. Chem. **57** (1985) 603.
3. L. D. Gelb, K. E. Gubbins, R. Radhakrishnan, and M. Sliwinska-Bartkowiak, Rep. Prog. Phys. **62** (1999) 1573.
4. D. H. Everett, in *The Solid Gas Interface*. E. A. Flood (Ed.), Marcel Dekker, New York (1967) Vol. 2, p. 1055.
5. W. F. Saam and M. W. Cole, Phys. Rev. B **11** (1975) 1086.
6. F. Celestini, Phys. Lett. A **228** (1997) 84.
7. A. Papadopoulou, F. van Swol, and U. M. B. Marconi, J. Chem. Phys. **97** (1992) 6942.
8. R. Evans, U. Marini Bettolo Marconi, and P. Tarazona, J. Chem. Phys. **84** (1986) 2376.
9. R. A. Guyer and K. R. McCall, Phys. Rev. B **54** (1996) 18.
10. G. Mason, Proc. R. Soc. London Ser. A **415** (1988) 453.
11. L. Sarkisov and P. A. Monson, Langmuir **17** (2001) 7600 and references therein.
12. J. H. Page, J. Liu, B. Abeles, H. W. Deckman, and D. A. Weitz, Phys. Rev. Lett. **71** (1993) 1216.
13. P. Huber and K. Knorr, Phys. Rev. B **60** (1999) 12 657.

14. D. Wallacher, N. Künzner, D. Kovalev, N. Knorr, and K. Knorr, Phys. Rev. Lett. **92** (2004) 195 704.
15. D. Stauffer and R. B. Pandey, J. Phys. A Math. Gen. **25** (1992) L1079.
16. M. C. Goh, W. I. Goldburg, and C. M. Knobler, Phys. Rev. Lett. **58** (1987) 1008.
17. S. B. Dierker and P. Wiltzius, Phys. Rev. Lett. **58** (1987) 1865.
18. M. Y. Lin, S. K. Sinha, J. M. Drake, X.-L. Wu, P. Thiyagrajan, and H. B. Stanley, Phys. Rev. Lett. **72** (1994) 2207.
19. F. Brochard and P. G. de Gennes, J. Phys. Lett. (Paris) **44** (1983) 785.
20. P. G. de Gennes, J. Phys. Chem. **88** (1984) 6469.
21. R. J. Birgeneau, R. A. Cowley, G. Shirane, and H. Yosthizawa, J. Stat. Phys. **34** (1984) 817.
22. L. Monette, A. J. Liu, and G. S. Grest, Phys. Rev. A **46** (1992) 7664; A. J. Liu, D. J. Durian, E. Herbolzheimer, and S. A. Safran, Phys. Rev. Lett. **65** (1990) 1897.
23. E. D. Siggia, Phys. Rev. A **20** (1979) 595.
24. I. M. Lifshitz and V. V. Slyozov, J. Phys. Chem. Solids **19** (1961) 35.
25. J. C. Lee, Phys. Rev. B **46** (1992) 8648.
26. M. Kardar, G. Parisi, and Y. C. Zhang, Phys. Rev. Lett. **56** (1986) 889.
27. R. Paul, S. Puri, and H. Rieger, Europhys. Lett. **68** (2004) 881.
28. R. Paul and H. Rieger, J. Chem. Phys. **123** (2005) 024 708.
29. P. C. Hohenberg and B. I. Halperin, Rev. Mod. Phys. **49** (1977) 435.
30. A. J. Bray, Adv. Phys. **51** (2002) 481.
31. J. M. Kosterlitz and D. J. Thouless, J. Phys. C **6** (1973) 1181; J. M. Kosterlitz, J. Phys. C **7** (1974) 1046.
32. D. J. Bishop and J. D. Reppy, Phys. Rev. Lett. **40** (1978) 1727.
33. I. Rudnick, Phys. Rev. Lett. **40** (1978) 1454.
34. M. R. Beasley, J. E. Mooij, and T. P. Orlando, Phys. Rev. Lett. **42** (1979) 1165.
35. B. I. Halperin and D. R. Nelson, Phys. Rev. Lett. **41** 121 (1978); D. R. Nelson and B. I. Halperin, Phys. Rev. B **19** (1979) 2457.
36. L. P. Regnault and J. Rossat-Mignod, in *Magnetic Properties of Layered Transition Metal Compounds*. L. J. deJongh (Ed.), Kluwer Academics Publ., Dordrecht (1990) p. 271.
37. M. Bretz, Phys. Rev. Lett. **38** (1977) 501.
38. Y. P. Feng and M. H. W. Chan, Phys. Rev. Lett. **71** (1993) 3822.
39. S. Fassbender, C. Steimer, D. Arndt, and K. Knorr, Phys. Rev. Lett. **75** (1995) 2526; Surf. Sci. **388** (1997) 201.
40. J. V. José, L. P. Kadanoff, S. Kirkpatrick, and D. R. Nelson, Phys. Rev. B **16** (1977) 1217.
41. D. H. Lee, J. D. Joannopoulos, J. W. Negele, and D. P. Landau, Phys. Rev. Lett. **52** (1984) 433; Phys. Rev. B **33** (1986) 450.
42. S. Lee and K.-C. Lee, Phys. Rev. B **49** (1994) 15 184; P. Olsson, Phys. Rev. Lett. **75** (1995) 2758; H.J. Xu and B. W. Southern, J. Phys. A **29** (1996) L133.
43. S. Teitel and C. Jayaprakash, Phys. Rev. B **27** (1983) 598.
44. M. Y. Choi and D. Stroud, Phys. Rev. B **32** (1985) 5773; M. Yosefin and E. Domany, Phys. Rev. B **32** (1985) 1778.
45. B. Berge, T. Diep, A. Ghazali, and P. Lallemand, Phys. Rev. B **34** (1986) 3177; H. Eikmans, J. E. van Himbergen, H. J. F. Knops, and J. M. Thijssen, Phys. Rev. B **39** (1989) 11 759.
46. J. Lee, J. M. Kosterlitz, and E. Granato, Phys. Rev. B **43** (1991) 11 531.
47. G. Ramirez-Santiago and J. V. José, Phys. Rev. Lett. **68** (1992) 1224; Phys. Rev. B **43** (1994) 11 531.
48. E. Granato and M. P. Nightingale, Phys. Rev. B **48** (1993) 7438.
49. Y. M. M. Knops, B. Nienhuis, H. J. F. Knops, and H. W. J. Blöte, Phys. Rev. B **52** (1994) 7402.

50. E. Granato, J. M. Kosterlitz, J. Lee, and M. P. Nightingale, Phys. Rev. Lett. **66** (1991) 1090.
51. M. P. Nightingale, E. Granato, and J. M. Kosterlitz, Phys. Rev. B **52** (1995) 7402.
52. G. S. Grest, Phys. Rev. B **39** (1989).
53. J.-R. Lee, Phys. Rev. B **49** (1994) 3317.
54. S. Lee and K.-C. Lee, Phys. Rev. B **49** (1994) 15 184.
55. S. Miyashita and H. Shiba, J. Phys. Soc. Jap. **53** (1984) 1145.
56. H.-J. Xu and B. W. Southern, J. Phys. A **29** (1996) L133.
57. S. Lee and K.-C. Lee, Phys. Rev. B **57** (1998) 8472.
58. G. S. Jeon, S. Y. Park, and M. Y. Choi, Phys. Rev. B **55** (1997) 14 088.
59. J. M. Kosterlitz and D. J. Thouless, J. Phys. C **6** (1973) 1181; J. M. Kosterlitz, *ibid.* **7** (1974) 1046.
60. P. Olsson, Phys. Rev. Lett. **75** (1995) 2758.
61. J. V. José and G. Ramirez-Santiago, Phys. Rev. Lett. **77** (1995) 4849; P. Olsson, Phys. Rev. Lett. **77** (1995) 4850.
62. E. H. Boubcheur and H. T. Diep, Phys. Rev. B **58** (1998) 5163.
63. D. Loison and P. Simon, Phys. Rev. B **61** (2000) 6114.
64. S. Faßbender, M. Enderle, K. Knorr, J. D. Noh, and H. Rieger, Phys. Rev. B **65** (2002) 165 411.
65. M. Itakura, J. Phys. Soc. Jpn. **70** (2001) 600.
66. M. S. S. Challa and D. P. Landau, Phys. Rev. B **33** (1986) 437.
67. J.-D. Noh, H. Rieger, M. Enderle and K. Knorr, Phys. Rev. E **65** (2002) 026 111.
68. E. Maus, Ph.D. thesis, Universität Mainz (1991).
69. K. Knorr, Phys. Rep. **214** (1992) 113.
70. K. Knorr, S. Faßbender, A. Warken, and D. Arndt, J. Low Temp. Phys. **111** (1998) 339.
71. S. W. Pierson, S. M. Ammirata, J. C. Hunnicutt, and L. A. Gorham, Phys. Rev. B **60** (1999) 1309.
72. J. L. Barrat, M. V. Feigelman, J. Kurchan, and J. Dalibard (Eds.), *Slow Relaxation and Nonequilibrium Dynamics in Condensed Matter*, Springer Berlin, Heidelberg, New York (2003).
73. G. Parisi, F. Ricci-Tersenghi, and J. J. Ruiz-Lorenzo, Eur. Phys. J. B **11** (1999) 317.
74. L. F. Cugliandolo, J. Kurchan, and G. Parisi, J. Phys. I (France) **4** (1994) 1641.
75. N. Kawashima and H. Rieger, *Recent Progress in Spin Glasses*. In *Frustrated Spin Systems*. H. T. Diep (Ed.), World Scientific, Singapure (2004); cond-mat/0312432.
76. D. A. Huse and C. L. Henley, Phys. Rev. Lett. **54** (1985) 2708.
77. D. Forster, D. R. Nelson, and M. J. Stephen, Phys. Rev. A **16** (1977) 732; D. A. Huse, C. L. Henley, and D. S. Fisher, Phys. Rev. Lett. **55** (1985) 2924.
78. R. Paul, S. Puri, and H. Rieger, Europhys. Lett. **68** (2004) 881; Phys. Rev. E **71** (2005) 061 109.
79. H. Rieger, B. Steckemetz, and M. Schreckenberg, Europhys. Lett. **27** (1994) 485; J. Kisker, L. Santen, M. Schreckenberg, and H. Rieger, Phys. Rev. B **53** (1996) 6418.
80. A. Hartmann and H. Rieger, *Optimization Algorithm in Physics*. Wiley VCH, Berlin (2002).
81. P. Nozières and F. Gallet, J. Phys. (Paris) **48** (1987) 353.
82. J. Toner and D. P. DiVincenzo, Phys. Rev. B **41** (1990) 632; Y.-C. Tsai and Y. Shapir, Phys. Rev. Lett. **69** (1992) 1773; Phys. Rev. B **50** (1994) 3546; T. Hwa and D. S. Fisher, Phys. Rev. Lett. **72** (1994) 2466.
83. Y. Y. Goldschmidt and B. Shaub, Nucl. Phys. B **251** (1985) 77.
84. G. Schehr and H. Rieger, Phys. Rev. B **71** (2005) 184 202.
85. C. Zeng, A. A. Middleton, and Y. Shapir, Phys. Rev. Lett. **77** (1996) 3204; H. Rieger and U. Blasum, Phys. Rev. B **55** (1997) R7394.